Multidisciplinary characterisation, weathering patterns, and durability assessment of stone blocks for the conservation of Tamentfoust fort (ex. Rusguniae) in Algiers

Nesrine Meddour, Boualem Djebri
Ecole Polytechnique d'Architecture et d'Urbanisme-Laboratoire Ville Architecture et Patrimoine –LVAP-EPAU-Algeria
n.meddour@epau-alger.edu.dz, https://orcid.org/0009-0002-2708-0680
djebrib@gmail.com, https://orcid.org/0000-0002-4819-8875

Luisa Rovero
Dipartimento di Architettura, University of Florence 50121, Italy
luisa.rovero@unifi.it, https://orcid.org/0000-0002-9484-855X

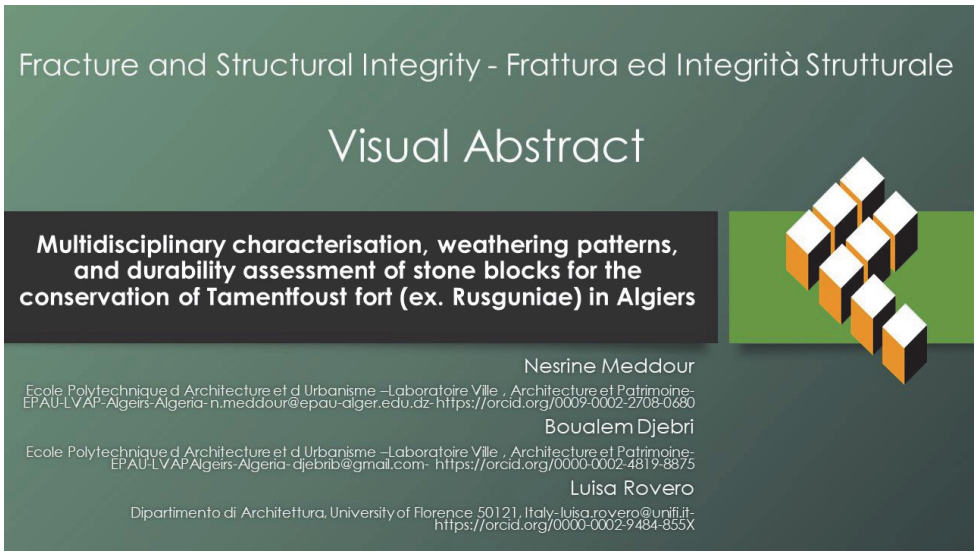

Citation: Meddour, N., Djebri, B., Rovero, L., Multidisciplinary characterisation, weathering patterns, and durability assessment of stone blocks for the conservation of Tamentfoust fort (ex. Rusguniae) in Algiers, Fracture and Structural Integrity, 74 (2025) 227-261.

Received: 15.07.2025
Accepted: 28.08.2025
Published: 04.09.2025
Issue: 10.2025

KEYWORDS: Stone building heritage, Conservation, chemical, Physical and mechanical characterisation, Durability and weathering mapping.

INTRODUCTION

The heritage represents the memory of the history and development of a country and should be preserved for new generations. The documentation and conservation of cultural heritage hold critical significance within scholarly and applied contexts. For stonework restoration projects, a rigorous understanding of construction materials and their intrinsic properties serves as an essential prerequisite for formulating effective intervention protocols [1]. Systematic evaluation of a monument's current state, particularly through analysis of the composition and conservation status of its

constituent materials across historical periods, represents a central objective in heritage building investigations. Such analyses provide pivotal insights for modern restoration efforts, while facilitating the assessment of prior conservation interventions in terms of long-term efficacy and material compatibility [2]. This methodological necessity acquires heightened urgency in regions such as Algeria, where some twentieth-century conservation practices utilized before, incompatible and harmful materials in conservation practices, such as composite matrices to treat deteriorated stone in heritage structures. These treatments were frequently applied without a prior experimentation, disregarding physicochemical compatibility with historical substrates, thereby accelerating material degradation. Many experimental studies have clearly demonstrated, that ill-suited consolidants, including polysiloxane resins and epoxy polymers, induce detrimental interfacial stresses and chemical modifications in treated stone surfaces [3]. The deterioration of stone monuments, driven by environmental and atmospheric factors, presents a global conservation challenge. Weathering processes, encompassing physical disintegration and chemical decomposition, are governed by interactions between lithic substrates and exogenic agents, including climate, biogenic activity, and pollutants. Numerous studies have explored techniques for assessing stone decay, exemplified by Fitzner's classification of nineteen weathering forms, which enables systematic mapping of façade degradation. Such methodologies facilitate precise quantification of weathering extent and damage severity, which is critical for informed conservation.

Historic military architecture represents a critical facet of cultural heritage, often bearing testimony to the technological, strategic, and social conditions of its time. The Ottoman fort of Tamentfoust is one of the emblematic monuments of the military fortification system heritage site, in the city of Algiers. Its preservation and enhancement are vital for safeguarding cultural identity and ensuring the structure's long-term stability. This important part of Mediterranean cultural heritage is, unfortunately, progressively being degraded due to weathering problems, necessitating a comprehensive study and complete documentation of the monument to assess its status. The Tamentfoust fort, located on the Mediterranean coast, is in a deplorable state of conservation, largely due to several causes such as the use of Portland cement-based mortars in prior restoration efforts. These mortars, incompatible with traditional materials like stone and lime-based mortars, have accelerated degradation by causing moisture accumulation, salt efflorescence, and cracking due to their rigidity and low vapor permeability effects, exacerbated by the saline marine environment. In stone buildings exposed to coastal conditions, cement mortars trap moisture and sea salts, leading to increased stone corrosion, joint disintegration, and loss of aesthetic authenticity. Research, such as that by Mahindad [4], demonstrates the efficacy of lime-based mortars combined with natural additives, such as olive oil and eggs, to enhance water repellency and reduce shrinkage. However, as it was noted in the same study that the documentation relating to the composition of old mortars in Algeria is not very rich, apart from some recent studies on the characterization of archaeological materials, which hinders long-term preservation efforts. Ouagueni in [5] advocates a shift toward locally sourced materials, such as natural hydraulic lime (NHL), later adopted in the restoration project of the citadel of Algiers and additives, like crushed bricks or vegetable fibers, to align with traditional construction techniques. This approach, supported by detailed physico-chemical analysis of historical mortars, ensures compatibility in terms of physical, chemical, and aesthetic properties while promoting sustainability through reduced environmental impact and the use of local resources. This paradigm shift underscores the urgent need for further research to develop repair mortars that respect the historical and cultural value of Algeria's built heritage, particularly for vulnerable structures like the Tamentfoust fort.

The scarcity of empirical data related to mechanical attributes and the precise architectural documentation of the construction materials, remains a recurring issue that also concerns the Tamentfoust fort. Therefore, through a multidisciplinary experimental investigation, the main purpose of the present study is to characterize the stone materials of the fort and to understand the degradation mechanisms affecting its external stone facades [6]. This integrated study was designed to inform conservation strategies with a robust scientific foundation, employing diagnostic techniques from geology, materials science, structural engineering, and conservation science [7]. The mineralogical and chemical composition of the stone materials was determined using X-ray diffraction (XRD) and X-ray fluorescence spectroscopy (XRF). Petrographic analysis using polarized light microscopy enabled the characterisation of textural features, mineral content, and alteration patterns. Micromorphological and compositional analyses were further conducted, using scanning electron microscopy coupled with energy-dispersive spectroscopy (SEM-EDX), facilitating high-resolution imaging of surface weathering phenomena. Physical and mechanical properties were quantified through measurements of apparent density and open porosity, as well as uniaxial compression and three-point bending tests to evaluate mechanical parameters. Water transport behaviour was assessed through capillary water absorption testing, which is an important indicator of stone vulnerability to moisture and associated decay processes. Durability was assessed by means of an accelerated aging test, which evaluates stone resistance to salt crystallization, one of the most destructive weathering mechanisms in porous materials. Non-destructive evaluations included ultrasonic pulse velocity testing, which offers insights into internal structural coherence, and infrared thermography to detect subsurface anomalies related to moisture

and detachment [8]. Monitoring of structural stability was carried out through the measurement of micro-cracks in external walls and patio gallery columns. Additionally, a laser scanning survey was employed to generate a high-resolution geometric model of the fort's façades, supporting both documentation and deformation analysis. The methodological framework adopted in this study enables a comprehensive understanding of the material characteristics and degradation patterns of the Tamentfoust fort, offering a scientific basis for the development of targeted, effective, and sustainable conservation measures. The novelty of this research lies in its pioneering investigation of the Tamentfoust fort, marking the first study to comprehensively characterize the physical and mechanical properties of its natural stone materials in a coastal environment, a critical endeavor given the monument's significant historical and architectural value. This originality is further enhanced by the combined use of destructive and non-destructive testing techniques tailored to this specific material, integrated with Terrestrial Laser Scanning (TLS) technology, which provides comprehensive graphical documentation previously unavailable [9] . This multidisciplinary approach offers an optimized and rapid method for the characterization of heritage stone in engineering applications, setting a new standard for the preservation and study of similar historical structures.

Figure 1: (a) external view (b, c) terrace (d) internal courtyard (e) aerial view (f) geographical location

HISTORICAL BACKGROUND OF TAMENTFOUST CITY

Tamentfoust, a key site for historical and architectural research, embodies a rich cultural evolution reflected in its changing names. Known as Rusguniae during Roman times, a name derived from the Phoenician "Rus"(meaning a bushy promontory) [10], it became Tamentfoust, meaning "hand" in the Tamazight language, during the Berber-Ottoman period. By the 14th century, Spanish influence renamed it Cap Matifou, and later, French colonial rule designated it Laperouse. Located 20 km east of Algiers along the eastern shore of the Bay of Algiers (Fig. 1), the city of Tamentfoust's defensive significance is evidenced by a network of fortifications, including Fort L'Empreur on the west coast of the bay of Algiers, and the Ottoman-era fort of Tamentfoust on the eastern side of the same bay [11]. Historical

records confirm Rusguniae was founded as a Roman colony by Augustus in 30 Before Common Era (BCE), later thriving as a Byzantine urban center [10]; [11]. Its orthogonal urban layout, covering 19 hectares, included two gateways (Fig. 2), with a north-eastern portal connecting to the Icosium-Tipasa trade route.

The 7th-century Arab conquest brought significant socio-religious changes. In the 12th century, the geographer Al-Idrīsī described Tamentfoust as "[...] a picturesque harbor beside ruins, with traces of temples and stone idols [...]"[10].A quarry, linked underground to Rusguniae's port, provided stone for Algiers' fortifications. Modern urban expansion has since obscured much of the site's archaeological remains, highlighting the urgent need for heritage preservation. The construction history of Tamentfoust's Ottoman fort is debated. Henri Klein dates its initial construction to 1661 under Ramadhan Agha, with further fortifications added after a 1685 bombardment [11]. In contrast, Georges Marçais argues for a 1722 foundation, citing French destruction in 1685 and subsequent rebuilding. This fort, strategically vital, anchored Algiers' defences at the eastern edge of the bay of Algiers. Salama in [11] identifies it as a model Ottoman coastal defence structure, built over Roman ruins (Rusguniae) to counter Spanish incursions and secure Mediterranean trade routes. Ottoman records highlight its importance during Khayr al-Din Barbarossa's rule. Al-Idrīsī's 12th-century account further notes Tamentfoust as "[...] a port nears a ruined settlement, preserving ancient relics [...]"[10]. After Ottoman revitalization, the site declined from the 18th century due to harbour siltation and Algiers' growing dominance.

The fort's architecture reflects a succession of cultural influences. Latin-inscribed spolia were incorporated into Ottoman masonry, while semi-circular bastions show Iberian design elements. Nineteenth-century excavations uncovered Ottoman ceramics alongside Roman column bases, providing evidence of continuous occupation. Despite 19th-century urban encroachment, the Cap Matifou ramparts endure as a testament to their military past, though locals have historically reused their stones.

Declared a national heritage site in 1967, the fort was converted into a museum in 1999. However, nearby urban development continues to threaten its preservation.

Figure 2: Main fort facades.

ARCHITECTURAL CHARACTERISTICS

The Ottoman fort of Tamentfoust is located at 36°48'23"N, 3°13'50"E, approximately 25 km east of Algiers. It is bordered primarily by the El Marsa massif to the north and east, and by the Mediterranean Sea to the south and west. The meteorological data including temperature, rainfall, humidity rate and wind speed, were obtained from the Algerian National Meteorological Office for the period 2006–2020 .These data were statistically analysed to identify monthly trends in temperature and precipitation, presented in two graphs, to highlight relationships between variables and distinguish dry and wet periods in the Bay of Algiers, *(Cf. Appendix A1).*

Strategically located at the eastern edge of Algiers Bay, the fort of Tamentfoust, exemplifies a distinctive architectural paradigm, within North Africa's defensive networks. Unlike typical Ottoman designs of the period, its octagonal morphology (28m diameter base) with a 3-meter-deep perimeter moat reflects advanced tactical engineering, enabling enhanced defender mobility and encirclement strategies. Access is provided through a southeastern drawbridge (5 × 1.5 m) leading to a postern gate. The 9-meter-high walls with a pronounced batter incorporate covered median and corner towers, equipped with arrow slits and loopholes. An upper terrace, with a parapet walkway, overlooks an arcaded central

courtyard, which houses functional spaces (kitchen, prayer hall, prison, hammam, and armory), accessible via a lateral staircase (Fig. 2). The 1992 restoration campaign identified multiple forms of deterioration, including: exfoliation, fissures, fractures, alveolar erosion, stone detachment, delamination, and rain-induced deposits, particularly in areas exposed to meteorological stressors such as solar radiation, saline aerosols, and humidity. Subsequent interventions in 2012 used cement-based mortars for façade repointing, a method criticized for its incompatibility with the fort's historical stone substrates.

THE GEOLOGY OF THE SITE

The stone deterioration mechanisms at Tamentfoust fort, are closely tied to the region's geological and structural context. The Algerian continental margin, part of the southern Mediterranean basin, is integrated into the internal domain of the Tellian Atlas chain [12]. Paleoanthropological investigations identify Ain Taya, located 6 km southwest of Tamentfoust's urban core, as a principal lithic source. Piroutet describes two stratigraphic horizons overlying Cartennien marls and Pliocene sands: a lower red sand stratum yielding Mousterian quartzite tools, and an upper greyish sand stratum, containing Neolithic flint artefacts. Piroutet further attributes the Roman-era quarrying of Tamentfoust's construction stones to Ain Taya. The Tertiary Miocene sequence, exposed eastward between Cap El Marsa and Bordj el Bahri, consists of Burdigalian marls with sandstone lenses and Vindobonian marly limestone's. Tectonic activity during this period, included Lower Miocene uplift of the Atlas range, and formation of the Mitidja-Cheliff synclinorium, followed by Middle Miocene extensional tectonics, volcanism, and the emergence of the Mitidja basin.

MATERIALS AND METHODS

Four stone blocks (E1, E3) as type T1 and (E2, E4) as type T2 with dimensions approximately of 17 × 37 × 15 cm, collected from the immediate surroundings of the fort , belong to the damaged masonry wall on the fort's terrace (Fig. 3). The blocks were cut into parallelepipedical specimens 30 × 5 × 5 cm, and cylindrical specimens via core drilling 50 mm bit (Fig. 5), (Fig. 6). For microscopic studies, thin sections were also prepared from the two blocks (Fig. 4). Stone samples were selected for their historical texture, avoiding contemporary materials to focus on the early construction phase, due to monument restorations in the 1992s and 2012. Below, are listed all the tests carried out, summarized in Tab. 1, with reference to the tested specimens.

Figure 3: Damaged masonry walls on the terrace where the stone block samples were taken.

- A micropalaeontological study on thin sections (Fig. 4) from sample T1-E1 and T2-E2, using an Olympus BX 43 microscope with 05 objectives (X2, X4, X10, X20 and X40) and an external 8 megapixel camera with cellSens image processing software, was conducted. The results are presented in the next paragraph and summarized in Tab. 2.
- X-ray diffraction (XRD) was used to analyse the mineralogical composition of four stone samples (PE1-3, PE1-5, PE2-6, PE2-4), identifying crystalline phases (e.g., magnesium-calcite, quartz) and their relative abundances via Bragg's law ($n\lambda=2d\sin\theta$) [2], *(Cf. Appendix A2-1)*.

Stone type	Block	Sample shape	Sample Name/Number	Type of analysis
T1	E1	Cylindrical	PE1(1-2-3-4-5-6)	D, Ca, Po, UCS, UWV, WA, Petr, XRD, XRF, SEM-EDX, Du-Cryst, Cra, Mpal
	E3	Cylindrical	PE3 (1-2-3-4-5-6)	D, Ca, Po, UCS, WA, Petr
T2	E2	Cylindrical	PE2 (1-2-3-4-5-6)	D, Ca, Po, UCS, WA, Petr, XRD, XRF, SEM-EDX, Cra ,Du-Acd, Mpal
	E4	Parallipipedic	PE4 (1-2-3)	D, Ca, Po, UWV,SHR, WA, Petr, FST

D=density, **Ca**=capillarity, **Po**=porosity, **UCS**=Uniaxial compressive strength, **UWV**=Ultrasonic wave velocity, **WA**=water absorption, **Petr**= Petrography, **Du-Cryst**= Durability test by salt crystallization, **Du-Acd**= Durability with accelerated ageing with HCl , **XRD**=X-ray diffraction, **XRF**= X-ray fluorescence, **SEM-EDX**=Scanning Electron Microscopy, **Cra**= Micro-cracks measurement, **SHR**= Schmidt hammer rebound, **FST**= Flexural strength test, **Mpal**= Micropaleontological study

Table 1: Samples description and the relative tests.

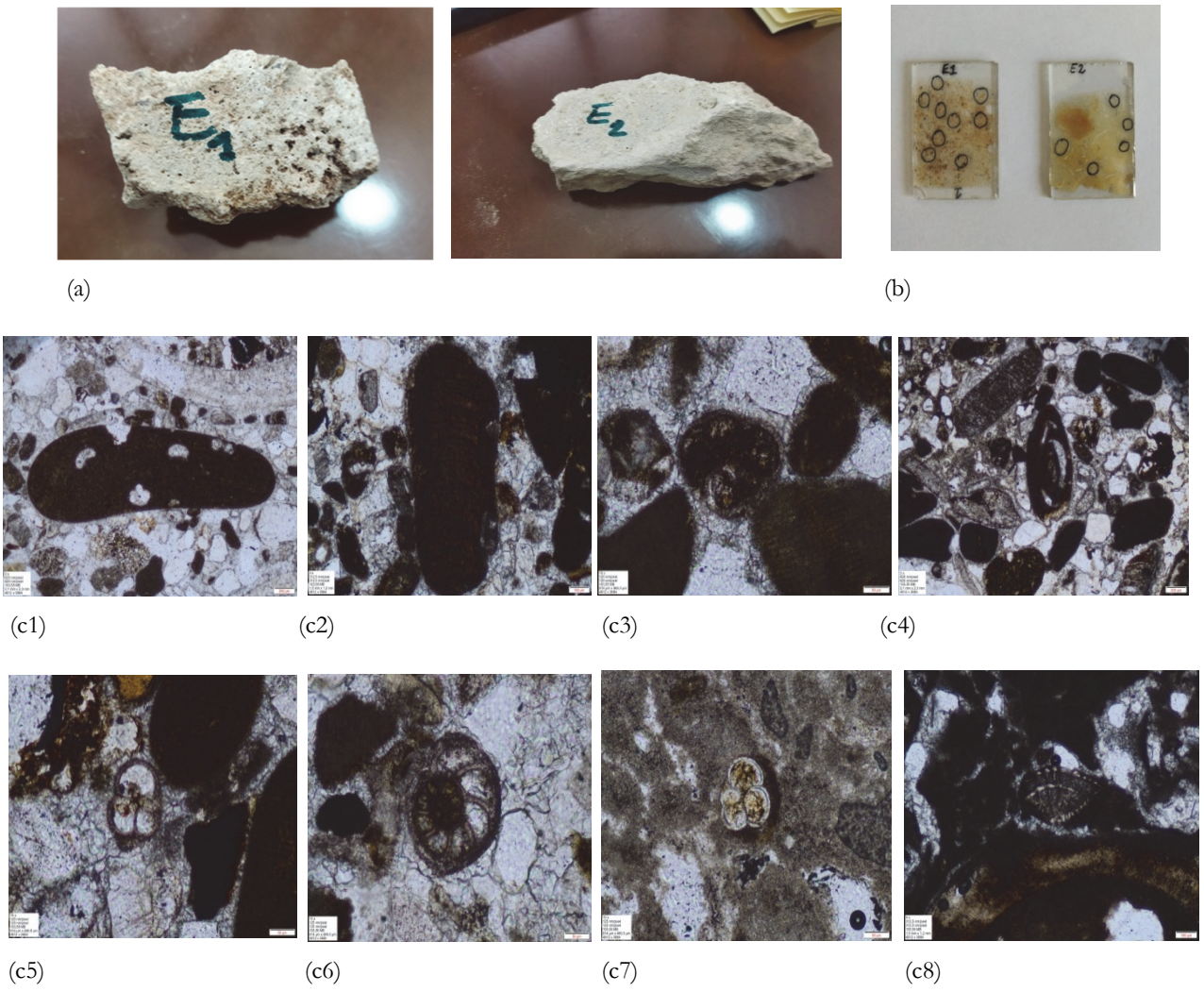

Figure 4: (a) the raw samples of the E1 and E2 stone type (b) thin section of two stone samples for a micropalaeontological study (c) micropaleontological results of the stone sample type E1 (From c1 to c6) and E2 (c7 and c8).

Stone sample	Description	Species encountered	N°	Mang	Dating
E1	Sandstone with red algae and bioclasts. The cement is carbonate, sometimes dolomitic to clayey in places.	Algae: ○ Lithophyllum phillipi ○ Mesophyllum laffitei Foraminifera: ○ Catapsydrax sp. ○ Miliolidae ○ Globigerinoides trilobus ○ Lituolidae ○ Globotruncanahilli (reworked Campanian-Maestrichtian form)	c2 c1 c3 c4 c5 c6	x4 x2 x10 x2 x10 x100	This sample is dated Miocene on the basis of the association of red algae and planktonic foraminifera, reworking a species from the Campano-Maestrichtian.
E2	Micrite with bioclasts and rare foraminifera	Foraminifera: ○ Globigerinoides sp. ○ Elphidium sp.	c7 c8	x10 x40	The age of this sample is Miocene.

Table 2: Results of micropalaeontological study of two stone types.

- Scanning electron microscopy coupled with energy dispersive Spectroscopy (SEM-EDX). This technique elucidated weathering mechanisms in heritage materials (*Cf. Appendix A2-2*).
- X-ray fluorescence spectrometry (XRF), is a technique which enabled precise qualitative and quantitative analysis of elemental concentrations (wt%) through calibration using certified reference materials, *(Cf. Appendix A2-3*).
- Petrographic analyses, using polarized light microscopy (Leitz ORTHOPLAN, 40–1000×), characterized the chemical and mineralogical composition of lithic specimens. These analyses revealed textural attributes, intragranular microporosity, bonding matrix integrity, and secondary mineralization phases, which are critical for understanding weathering mechanisms in heritage materials), *(Cf. Appendix A2-4).*
- Open porosity (po %) of cylindrical stone samples were measured by hydrostatic weighing per EN 1936 [13], *(Cf. Appendix A2-5).*
- Water absorption by atmospheric pressure (Ab) for stone samples was performed according to EN 13755 (2008), *(Cf. Appendix A2-6).*
- Capillary water absorption (C) in stone samples was evaluated according to EN 1925 (2000) (*Cf. Appendix A2-7).*
- An accelerated aging experiment conducted per EN 12370 (1999), assessed the durability of the stone samples against salt crystallization [14], *(Cf. Appendix A2-8).*
- An accelerated aging experiment, conducted per EN 12371 (2001), evaluated the durability of T2 stone samples from block E2 under hydrochloric acid (HCl) exposure, substituting for sulphur dioxide (SO2) [15],[16],*(Cf. Appendix A2-9).*
- Ultrasonic pulse velocity (Vp) was measured on T1 and T2 stone samples from blocks E1 and E2 per EN 14579 (2005) [17], *(Cf. Appendix A2-10).*
- Infrared thermography was applied to the fort's exterior and interior to detect structural anomalies (cracks, water infiltrations, delamination, voids, and inclusions), thermal bridges, and condensation zones. [17],[18], *(Cf. Appendix A2-11).*
- The Schmidt hammer rebound test, performed with a Proceq type N instrument, assessed the surface hardness and integrity of T2 stone samples from block E4, per ASTM D5873, *(Cf. Appendix A2-12).*
- Uniaxial compressive strength (σc) of non-altered and altered stone samples (E1–E3 from T1; E2 from T2) was measured according to EN 1926 (2006), *(Cf. Appendix A2-13).*
- Flexural strength (σf) of plate-shaped stone specimens (30 × 5 × 5 cm) was measured according to EN 12372 (2006), *(Cf. Appendix A2-13).*
- Micro-cracks development in the external walls and columns supporting the patio gallery, were monitored over 30 days from 19/09/2024. Additionally, microstructural changes in four stone samples were analysed before and after aging durability tests to assess surface alterations due to mineralogical reactions, *(Cf. Appendix A2-14).*
- Terrestrial laser scanning enabled precise stonework mapping and project management captured geometric data of the Ottoman fort's façade across 40 scan positions. This technique facilitates the mapping of weathering patterns and lithological characterisation. High-resolution orthophotos complemented the dataset, informing conservation strategies [19],[20], [21],*(Cf. Appendix A2-15).*

Figure 5: Stone samples and extracted cylindrical specimens.

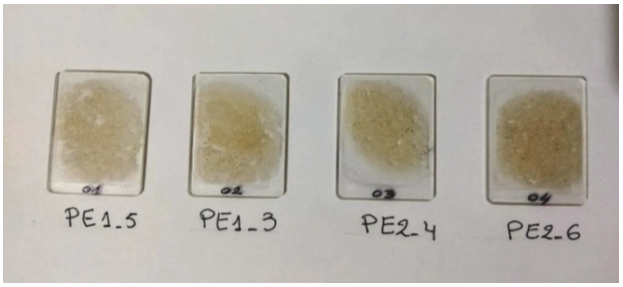

Figure 6: Thin sections for petrographic analysis.

RESULTS AND DISCUSSION

Petrographic analysis

Petrographical examination revealed that the stone sample PE1-5 T1 was a white to beige sedimentary rock with a massive structure and grainstone texture, according to Dunham's classification. It is a fossiliferous limestone composed mainly of carbonate cement containing fossiliferous and detrital material (Fig. 7a, photomicrograph of thin section 01 showing plagioclase, quartz, microcline, and biotite under cross-polarized light at 6.3x magnification). The light-coloured cement is formed by microsparite calcite with an average size of 0.05 mm, occupying around 50% of the total volume of the rock (Fig. 7b, photomicrograph of thin section 01 showing fossils and quartz under cross- polarized light at 6.3x magnification). The rock is characterized by the presence of fossils of various shapes and sizes ranging from 0.05 to 0.6 mm, with tests that are generally whole to occasionally fragmented. Some fossils are recrystallized by secondary calcite. Detrital material is represented by disseminated quartz grains, angular in shape and varying in size from 0.05 to 0.5 mm (Fig. 7c, photomicrograph of thin section 01 showing muscovite under cross-polarized light at 6.3x magnification). The feldspars are represented by elongated plagioclases varying in size from 0.05 to 0.1 mm. The microcline is also distinguished by its squared-off macles. Biotite is rarely seen, in the form of lamellae averaging 0.3 mm in size. Muscovite appears as fine rods, ranging in size from 0.05 to 0.2 mm. Opaque minerals are poorly represented, showing isolated grains of automorphic form and ranging in size from 0.05 to 0.1mm. Porosity is marked by the presence of voids sometimes recrystallized by secondary calcite Tab. 3.

For the sample PE_2-6 (T2) the petrographic study summarised in Tab. 4, shows that it's a fossiliferous limestone with a massive structure and grainstone texture (Fig. 8a, photomicrograph of thin section 04 showing fossils and quartz under cross-polarized light at 6.3x magnification). It is composed mainly of carbonate cement containing fossils, as well as

feldspar, quartz, chlorite and muscovite (Fig. 8b), photomicrograph of thin section 04 showing fossils under cross-polarized light at 6.3x magnification). The cement covers around 40% of the total volume of the rock and takes the form of a microspartic composed of calcite averaging 0.05 mm in size (Fig. 8c), photomicrograph of thin section 04 showing Muscovite under cross-polarized light at 10x magnification).

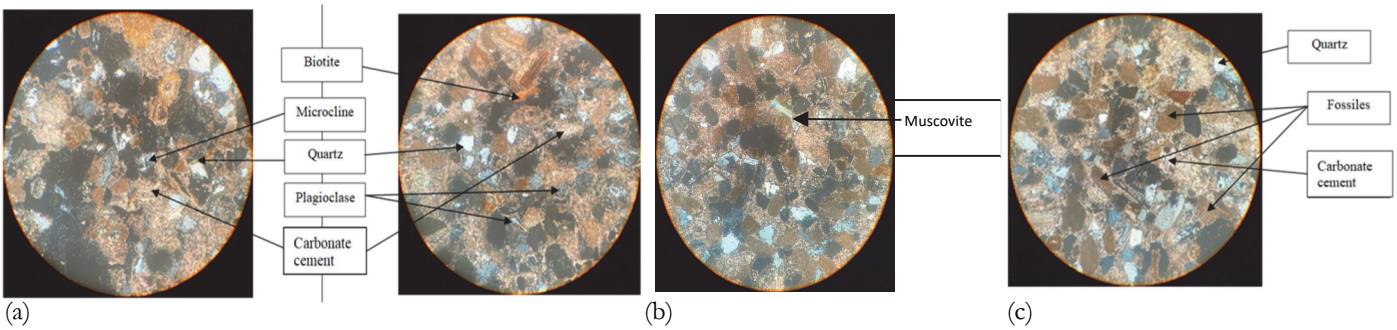

Figure 7: Petrographic study of thin section for sample PE1-5 (T1).

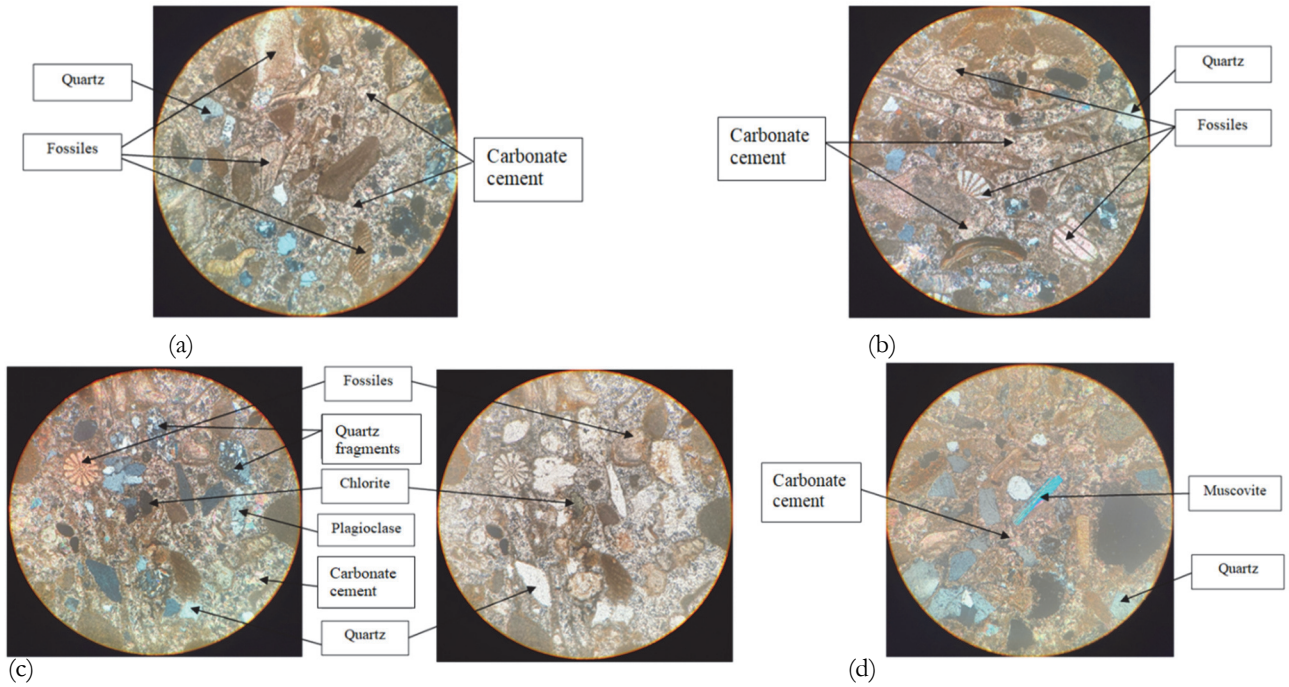

Figure 8: Petrographic study of thin section for sample PE2-6 (T6).

Fossils are widespread in the rock, showing various forms of nummulites, radiolarians, orbitolites, etc. with whole or sometimes fragmented tests filled with secondary calcite, up to 1 mm in size. Feldspars are represented by plagioclases in the form of small elongated patches showing clearly visible polysynthetic macles with an average size of 0.2 mm, noting the presence of the elongated perthitic orthoclase and the very common microcline, clearly distinguished with its squared macle. Quartz occurs in angular grains ranging in size from 0.05 to 0.5 mm.

There are a few quartz clasts, which are generally polycrystalline, represented by crystals that are well interlocked with one another and up to 3 mm in size. Fine chlorite lamellae are observed, with a greenish colour and a size that varies from 0.05 to 0.2 mm. Muscovite occurs in the form of rods averaging 0.4 mm in size. The opaque minerals show small isolated grains of automorphic shape and 0.05 to 0.1 mm in size (Fig. 8d, photomicrographs of thin section 04 showing fossils, quartz, plagioclase, and chlorite under cross-polarized light and plane-polarized light at 10x magnification). The rock has a few notable voids and microcracks, reflecting its porosity.

Mineralogical composition	Content in %	Grains form	Grains dimensions (mm)
Calcite	50	Xenomorph	0.05
Fossils	28	Various	0.1-0.6
Quartz	16	Angular	0.05-0.5
Plagioclase	01	Elongated	0.05-0.1
Microcline	01	Xenomorph	0.05-0.1
Muscovite	01	Rod	0.05-0.2
Biotite	01	Lamellar	0.3
Opaque minerals	01	Automorph	0.05-0.1
Iron hydroxides	01	Coating	-

Table 3: Petrographic study results for sample PE1-5 (T1).

Mineralogical composition	Content in %	Grains form	Grains dimensions (mm)
Calcite	40	Cement	0.05
Fossils	35	Various	0.1-1
Quartz	15	Angular	0.1-3
Plagioclase	03	Elongated	0.05-0.2
Microcline	01	Xenomorphic	0.05-0.1
Orthoclase	01	Elongated	0.05-0.3
Chlorite	01	Lamellar	0.05-0.2
Muscovite	01	Rod	0.05-0.4
Opaque minerals	01	Automorph	0.05-0.1
Iron hydroxides	01	Plaster	-

Table 4: Petrographic study results for sample PE2-6 (T2).

The fort stone sample PE1-3 subjected to crystallisation test, a light-colored fossiliferous limestone with a massive grainstone structure, consists of 50% microsparite calcite cement (<0.1 mm), 30% fossils (up to 0.6 mm, various shapes), quartz (0.05–0.5 mm, angular), elongated plagioclases (0.1 mm), xenomorphic microcline (0.1 mm, grid-pattern macles), micas (biotite lamellae 0.1–0.4 mm, muscovite 0.2 mm), rare automorphic opaque minerals (0.05–0.1 mm), and reddish iron hydroxide coatings Tab. 5, (Fig. 9). Calcite dissolution by Cl^- ions weakens the cement, reducing matrix cohesion, resulting in a modest mass loss (ΔM :0.65%) and a compressive strength (σ_c) reduction of <10%, indicating minimal surface degradation. Moderate porosity, inferred from 1% iron hydroxides and EDX-detected oxygen content pores (70.20 atom %), may amplify cyclic damage under salt-induced stress. However, partial pore obstruction by hydroxides limits connectivity, mitigating strength loss. The heterogeneous microstructure, with microfossils and cement as primary crack initiation sites, increases susceptibility to cyclic deterioration due to porosity and mineral variability.

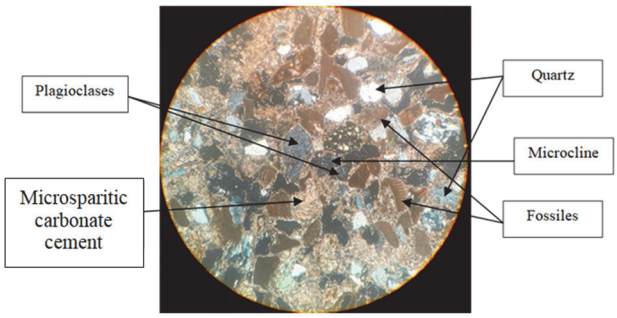

Figure 9: Petrography analysis-Microscopic photograph of thin section 02 of the sample PE1-3 under LPA GX6.3.

Mineralogical composition	Content in %	Grains form	Grains dimensions (mm)
Calcite	50	Xenomorph	0.05
Fossils	30	Various	0.1-0.6
Quartz	14	Angular	0.05-0.5
Plagioclase	01	Elongated	0.05-0.1
Microcline	01	Xenomorph	0.05-0.1
Muscovite	01	Rod	0.05-0.2
Biotite	01	Lamellar	0.1-0.4
Opaque minerals	01	Automorph	0.05-0.1
Iron hydroxides	01	Coating	-

Table 5: Petrographic study results for sample PE1-3 (T1).

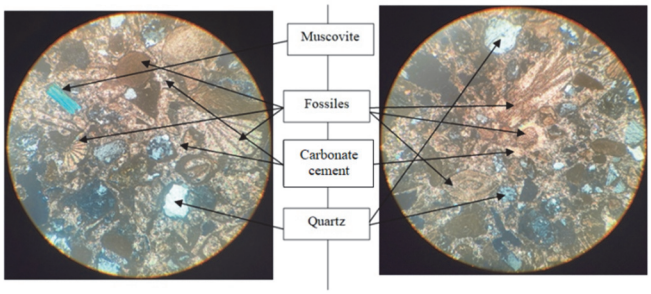

Figure 10: Microscopic photographs of thin section 03 of the sample PE2-4, displaying fossils, quartz, and muscovite under LPA GX6.3.

Mineralogical composition	Content in %	Grains form	Grains dimensions (mm)
Calcite	50	Cement	0.05
Fossils	30	Various	0.1-1.5
Quartz	15	Angular	0.05-0.5
Plagioclase	01	Elongated	0.05-0.2
Microcline	01	Xenomorph	0.05-0.1
Muscovite	01	Rod	0.05-0.4
Opaque minerals	01	Automorph	0.05-0.1
Iron hydroxides	01	Coating	-

Table 6: Petrographic study results for sample PE2-4 (T2).

Petrographic analysis after ageing test with HCl, of the T2-type stone sample PE2-4 summarised in Tab. 6 revealed a sedimentary rock with a massive structure and grainstone texture. It is a fossiliferous limestone, consisting of a carbonate matrix containing abundant fossiliferous material. The cement has a light background and is formed by microsparite calcite with an average size of 0.05 mm (Fig. 10)**.** Calcite occupies approximately 50% of the total rock volume. Fossils are relatively abundant, in various forms (Nummulites, Orbitolites, etc.), up to 1.5 mm in size. These fossils have intact tests and are recrystallized by secondary calcite. The detrital material contains quartz, sometimes disseminated in angular form, ranging in size from 0.05 to 0.1 mm. Disseminated plagioclase is elongated and averages 0.2 mm in size. Microcline is present in a grid pattern, 0.1 mm in size. Muscovite rods are observed, varying in size from 0.05 to 0.4 mm. Opaque minerals are automorphic and vary in size from 0.05 to 0.1 mm. Iron hydroxides appear as a reddish coating. The rock is characterized by voids that are rarely recrystallized by secondary calcite. Post-test petrography revealed etched calcite grains, increased porosity, and potential microcracking. XRD analysis revealed reduced calcite peaks and increased amorphous phases due to dissolution processes (Fig. 11). Quartz and silicate peaks remain stable, while XRF and EDX

analyses, reported in Tab. 8 and Tab. 12, respectively, showed a decrease in calcium content and an increase in chlorine, attributed to HCl reaction products, with stable silicon and other silicate-related elements, confirming the stone's chemical alteration under acidic conditions. The predominant chemical process involves the dissolution of carbonate minerals. The interaction of HCl with stone is primarily attributed to chemical reactions between this atmospheric pollutant and calcium-bearing minerals within the stone matrix, such as calcite, dolomite, plagioclase, and actinolite. Even in stones with minimal or no intrinsic calcium content, calcium ions may originate from exogenous sources, including adjacent lime-based mortars, calcareous building materials, or atmospheric particulate deposition.

Chemical analysis

XRF, XRD, and EDX were used to characterize stone samples PE1-5 (T1) and PE2-6 (T2) from Tamentfoust fort, revealing a carbonate-silicate composition with potential metamorphic or igneous origins [21]. XRF analysis identified major and trace elements, including calcium (23.53–25.00%), silicon (5.85–6.32%), iron (0.808%), and manganese (0.015%) Tab. 7. XRD analysis detected crystalline phases, such as dolomite ($CaMg(CO_3)_2$), quartz (SiO_2), pyroxene ($(Mg,Fe)SiO_3$), muscovite, cristobalite, and sylvanite, with PE2-6 showing similar mineralogy but with magnesium-calcium carbonate versus magnesian calcite in PE1-5 (Fig. 11). EDX analysis Tab. 9, confirmed higher surface calcium (34.51–35.49%) and silicon (9.36–10.67%), validating XRF results, and indicated micro-inhomogeneities, low heavy metal contamination (copper, zinc, lead), and high oxygen content (54.82%), supporting carbonate-silicate structures . Sample PE2-6 exhibited slightly higher calcium and aluminum, plus titanium (absent in PE1-5) and elevated manganese, while PE1-5 had marginally more silicon; iron content remained comparable. Trace elements, such as sulfur, showed minor variations. Low toxic element levels (lead, arsenic) ensure safety for applications, particularly for PE2-6. With calcite content below 40**%** (Tab. 10, Fig. 12), ISRM standards indicate that no consolidation treatments are required.

After the salt crystallisation test, the elevated oxygen content (50.50 wt%)was recorded on the T1 litotype sample PE1-3. This result indicates the dominance of oxygen-rich minerals, such as silicates and carbonates, which may increase porosity and chemical susceptibility to NaCl crystallization damage. Chemical processes involve NaCl dissolution in water: $NaCl(s) \rightarrow Na^+(aq) + Cl^-(aq)$. This is followed by recrystallization upon evaporation, where Na^+ and Cl^- recombine into NaCl crystals within pores, generating internal pressure and mechanical damage. Additionally, under humid conditions with CO_2, carbonate interactions occur: $CaCO_3(s) + 2NaCl(aq) + CO_2(g) + H_2O(l) \rightarrow CaCl_2(aq) + 2NaHCO_3(aq)$.

The T2 lithotype sample PE2-4, a calcite-dominated limestone with fossil inclusions, exhibits significant reactivity to hydrochloric acid (HCl), evidenced by CO_2 liberation. Silicate minerals (quartz, feldspars, and micas) show robust resistance to acidic and aqueous degradation but undergo protracted clay-phase alteration. Opaque phases and ferric hydroxides, such as pyrite (FeS_2) and goethite ($FeO(OH)$), demonstrate minimal acid reactivity, though oxidative transformation occurs in hydrated, oxygenated systems. Pyrite reacts with HCl to produce $FeCl_2$ and toxic H_2S gas via: $FeS_2(s) + 2HCl(aq) \rightarrow FeCl_2(aq) + H_2S(g)$. Ferric hydroxides (e.g., goethite) dissolve under HCl exposure:
$FeO(OH)(s) + 3HCl(aq) \rightarrow FeCl_3(aq) + 2H_2O(l)$. Calcite reacts vigorously with HCl, generating CO_2, H_2O, and soluble $CaCl_2$: $CaCO_3(s) + 2HCl(aq) \rightarrow CaCl_2(aq) + CO_2(g) + H_2O(l)$. Hydrolytic feldspar degradation contrasts sharply with quartz, which exhibits negligible dissolution kinetics in acidic, calcium-rich environments. Primary silicates (feldspars, micas, chlorites) are susceptible to gaseous HCl in hydrated conditions, with plagioclases ($NaAlSi_3O_8$–$CaAl_2Si_2O_8$) releasing cationic species (Ca^{2+}, K^+, Na^+, Mg^{2+}, $Fe^{2+/3+}$) under HCl-polluted humidity, forming soluble derivatives. Acidic hydrolysis of feldspars yields secondary kaolinite-dominated clay matrices, underscoring the interplay between mineralogy, atmospheric pollutants, and long-term lithological alteration. This reaction can be expressed as:

$$CaAl_2Si_2O_8(s) + 8HCl(aq) \rightarrow CaCl_2(aq) + 2AlCl_3(aq) + 2SiO_2(s) + 4H_2O(l).$$

Superficial alteration, involving water and CO_2, results in transformation into clays (e.g., kaolinite), affecting minerals such as microcline ($KAlSi_3O_8$), orthoclase ($KAlSi_3O_8$), and muscovite ($KAl_2(AlSi_3O_{10})(OH)_2$). The stone, composed of 40% calcite, 35% fossils, 15% quartz, and minor silicates, showed calcite dissolution (0.05 mm grains) causing grain detachment and structural instability, while quartz and silicates (angular or elongated) remained largely unreactive Tab. 6.

Fossil morphology increased localized porosity (*po*: 8.59%), with SEM revealing cavities and pores (30–50 μm) from calcite and fossil dissolution, weakening structural integrity. Uniaxial compressive strength (σ_c) decreased from 27.57 MPa to 17.94 MPa, with microcracks and fractured grains indicating mechanical degradation. HCl exposure caused yellow-brown surface discoloration from iron enrichment (0.805% ± 0.012% by XRF), though EDX failed to detect iron due to detection limits or spectral interference. Potential oolites (grain size 0.05–3 mm) suggest additional matrix vulnerabilities. Calcite (40%) and iron hydroxide (1%) dissolution exposed the silicate matrix, producing coloured residues (hydrated iron

oxides), while quartz remained stable. Calcite dissolution increased porosity (p_0), creating voids, reducing bulk density (ρ_b) (potentially from 2.7 g/cm³ to 2.4 g/cm³ with 10% calcareous loss), and facilitating water, salt, or pollutant infiltration, accelerating weathering. Localized dissolution induced mechanical stresses, microcracks, and $CaCl_2$ crystallization, exacerbated by CO_2 gas bubble formation, with surface roughness increasing due to differential dissolution and iron hydroxide oxidation causing rusty hues. These changes increased porosity (p_0), brittleness, and reduced durability, particularly in humid or polluted environments, necessitating less aggressive conservation methods, such as weak acids or mechanical cleaning.

The reported zero error margins (±0.000%) for certain elements (e.g., Zn, Pb, Rb, Zr, As, Y, and L.E.) arise from the specifications of the SciAps X-200 XRF spectrometer. For trace elements, concentrations at or below the instrument's limit of detection (typically <0.01%) yield negligible uncertainty at the reported resolution. For light elements (L.E.), values are estimated by difference, producing no measurable statistical uncertainty.

Content in %	Sample	
	P-E1-5	P-E2-6
Light Element (LE)	67.35%$^{+/-0,000\%}$	65.61%$^{+/-0,000\%}$
Silicon (Si)	6.32%$^{+/-0,037\%}$	5.85%$^{+/-0,036\%}$
Sulfur (S)	0.097%$^{+/-0,003\%}$	0.116%$^{+/-0,003\%}$
Calcium (Ca)	23.53%$^{+/-0,023\%}$	25.00%$^{+/-0,025\%}$
Iron (Fe)	0.808%$^{+/-0,012\%}$	0.805%$^{+/-0,012\%}$
Zinc (Zn)	0.003%$^{+/-0,000\%}$	0.003%$^{+/-0,000\%}$
Strontium (Sr)	0.029%$^{+/-0,000\%}$	0.032%$^{+/-0,001\%}$
Lead (Pb)	0.002%$^{+/-0,000\%}$	0.002%$^{+/-0,000\%}$
Aluminium (Al)	1.40%$^{+/-0,038\%}$	1.99%$^{+/-0,043\%}$
Phosphorus (P)	0.226%$^{+/-0,006\%}$	0.172%$^{+/-0,005\%}$
Potassium (K)	0.204%$^{+/-0,003\%}$	0.315%$^{+/-0,003\%}$
Manganese (Mn)	0.015%$^{+/-0,002\%}$	0.050%$^{+/-0,004\%}$
Copper (Cu)	0.008%$^{+/-0,001\%}$	0.002%$^{+/-0,000\%}$
Rubidium (Rb)	0.001%$^{+/-0,000\%}$	0.003%$^{+/-0,000\%}$
Zirconium (Zr)	0.001%$^{+/-0,000\%}$	0.003%$^{+/-0,000\%}$
Nickel (Ni)	0.004%$^{+/-0,001\%}$	-
Arsenic (As)	0.001%$^{+/-0,000\%}$	-
Yttrium (Y)	-	-
Titanium (Ti)	-	0.047%$^{+/-0,013\%}$

Table 7: XRF analysis of samples PE1-5 (T1) and PE2-6 (T2).

Content in %	Sample	
	P-E2-4	P-E1-3
Light Element (LE)	65.97%$^{+/-0,000\%}$	69.42%$^{+/-0,000\%}$
Silicon (Si)	5.70%$^{+/-0,038\%}$	6.67%$^{+/-0,037\%}$
Sulfur (S)	0.048%$^{+/-0,003\%}$	0.245%$^{+/-0,004\%}$
Calcium (Ca)	24.94%$^{+/-0,025\%}$	21.12%$^{+/-0,021\%}$
Iron (Fe)	0.987%$^{+/-0,013\%}$	0.581%$^{+/-0,011\%}$
Zinc (Zn)	0.003%$^{+/-0,000\%}$	0.011%$^{+/-0,001\%}$
Strontium (Sr)	0.030%$^{+/-0,000\%}$	0.031%$^{+/-0,001\%}$
Lead (Pb)	0.003%$^{+/-0,000\%}$	0.002%$^{+/-0,000\%}$
Aluminium (Al)	1.82%$^{+/-0,045\%}$	1.51%$^{+/-0,037\%}$
Phosphorus (P)	0.157%$^{+/-0,006\%}$	0.240%$^{+/-0,006\%}$
Potassium (K)	0.240%$^{+/-0,003\%}$	0.159%$^{+/-0,002\%}$
Manganese (Mn)	0.026%$^{+/-0,003\%}$	0.016%$^{+/-0,003\%}$
Copper (Cu)	0.002% $^{+/-0,000\%}$	0.006%$^{+/-0,001\%}$
Rubidium (Rb)	0.002%$^{+/-0,000\%}$	0.001%$^{+/-0,000\%}$
Zirconium (Zr)	0.003%$^{+/-0,000\%}$	0.002%$^{+/-0,000\%}$
Nickel (Ni)	-	-
Arsenic (As)	-	-
Yttrium (Y)	0.001%$^{+/-0,000\%}$	-
Titanium (Ti)	0.068%$^{+/-0,014\%}$	-

Table 8: XRF analysis of samples PE1-3 (T1) and PE2-4 (T2).

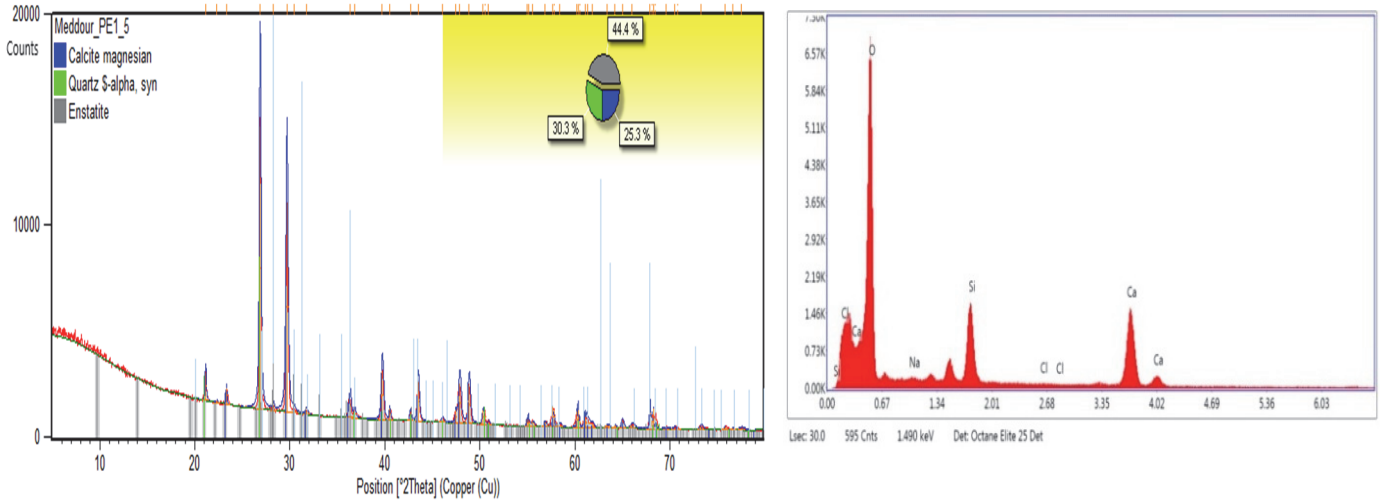

Figure 11: XRD and EDX analysis of sample PE1-5 (T1).

Element	Weight %	Atomic %	Error %
O	54.82	73.57	8.75
Na	0.21	0.20	62.88
Si	9.36	7.16	4.30
Cl	0.11	0.07	62.33
Ca	35.49	19.01	4.05

Table 9: Determination of chemical composition using EDX for sample PE1-5 (T1).

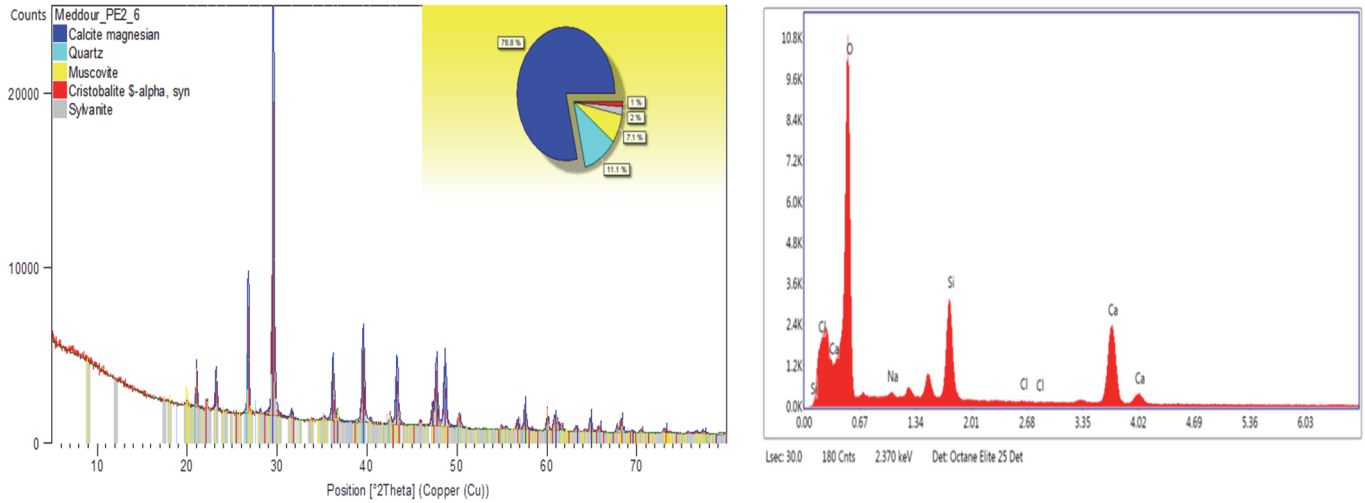

Figure 12: XRD and EDX analysis of sample PE2-6 (T2).

Element	Weight %	Atomic %	Error %
O	54.42	73.02	8.75
Na	0.31	0.29	29.94
Si	10.67	8.15	4.09
Cl	0.09	0.05	61.49
Ca	34.51	18.48	3.79

Table 10: Determination of chemical composition using EDX of the sample PE2-6 (T2).

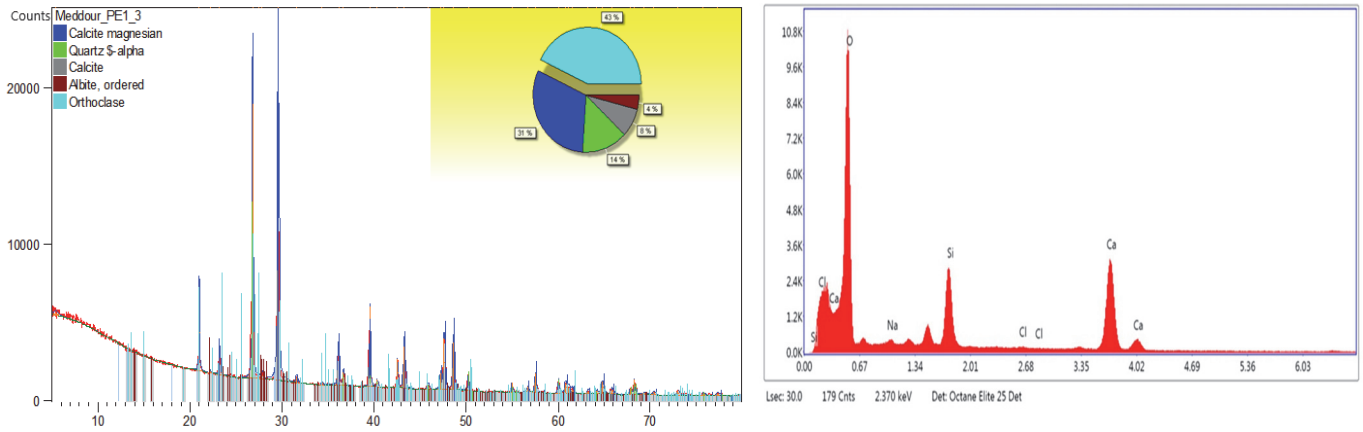

Figure 13: XRD and EDX analysis graphs of the sample PE1-3 (T1).

Element	Weight %	Atomic %	Error %
O	50.50	70.20	8.93
Na	0.52	0.50	17.42
Si	8.81	6.98	4.03
Cl	0.43	0.27	28.83
Ca	39.74	22.05	3.67

Table 11: Determination of chemical composition using the EDX technique of the sample PE1-3 (T1).

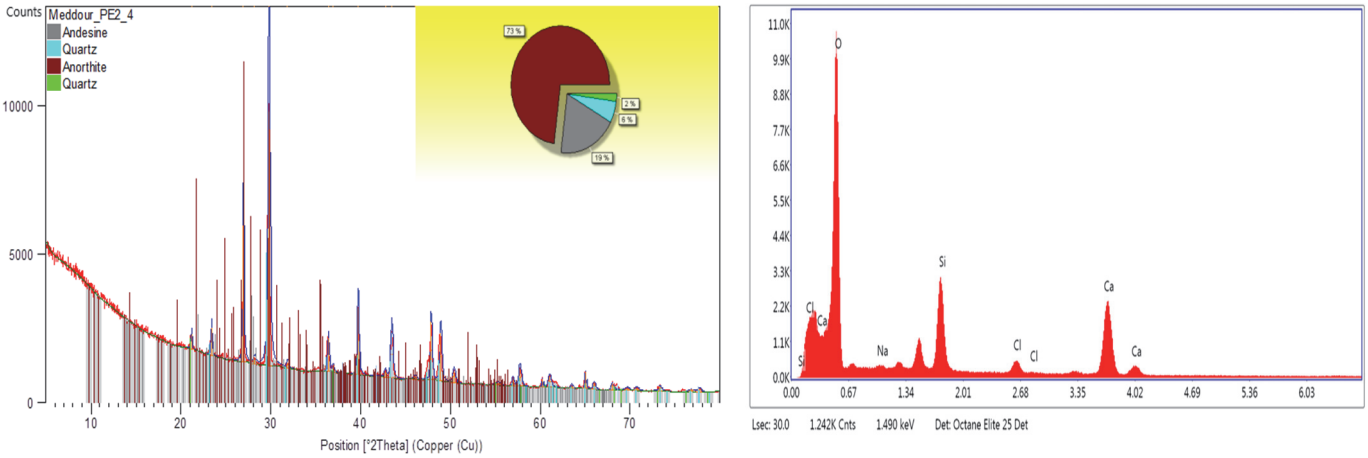

Figure 14: XRD and EDX analysis graph of the sample PE2-4 (T2).

Element	Weight %	Atomic %	Error %
O	53.28	72.10	8.74
Na	0.24	0.22	47.75
Si	10.37	7.99	3.99
Cl	2.49	1.52	9.99
Ca	33.63	18.17	3.82

Table 12: Determination of chemical composition using the EDX technique of the sample PE2-4 (T2).

SEM analysis

SEM-EDX analyses of limestone samples identified a composition of oxygen (50.50 wt%), calcium (39.74 wt%), silicon (8.81 wt%), sodium (0.52 wt%), and chlorine (0.43 wt%) Fig. 13, Tab. 11. The presence of sodium (Na) and chlorine (Cl) confirms NaCl, indicative of salt crystallization, while silicon and calcium suggest silicates (SiO_2) and carbonates ($CaCO_3$), respectively. The high calcium content supports the classification of the stone as limestone, which is susceptible to salt-induced deterioration. Salt crystallization tests on T1 limestone samples from Tamentfoust fort elucidated intricate chemical and mechanical degradation processes driven by saline interactions under varying environmental conditions. NaCl reactions produce highly soluble $CaCl_2$ and $NaHCO_3$, which leach from the stone, compromising structural integrity, with the extent of deterioration modulated by humidity, temperature, and ion presence. Silicates (SiO_2), while chemically resistant to direct NaCl interactions, undergo slow hydrolytic alteration in aqueous environments with additional ions, forming clay minerals or hydrated silicates, contributing to gradual long-term degradation. The mechanical impact of NaCl crystallization within pores exerts internal pressures of 2–5 MPa (lower than Na_2SO_4's 10–20 MPa), inducing microcracking and stone disintegration, amplified by repetitive dissolution-crystallization cycles, resulting in significant mechanical damage over time. SEM analysis at 200× (30 µm) (Fig. 15a) reveals a calcite-dominated matrix (50%) with 30% elongated or irregular fossils (50–200 µm) and angular quartz/feldspar grains (confirmed by XRD), characterized by a uniform, mildly porous cement texture (pores <5 µm) from low-compaction sedimentary origins. Sparse sub-parallel microcracks (10–20 µm) suggest preparation-induced or internal stresses, with minimal mass loss (ΔM:

0.65%) and no visible NaCl crystals, indicating limited surface degradation. At 2.20k× (3 µm) (Fig. 15f), heterogeneously distributed nanometric pores (0.2–0.8 µm), some occluded by iron hydroxides (bright contrast), are typical of limestone, facilitating saline solution penetration and increasing vulnerability to salt-induced damage. Calcite surfaces exhibit "honeycomb" dissolution streaks from Cl^- ion activity, while quartz remains uncorroded, reflecting its chemical resilience. A fine intergranular microcrack (<0.1 µm) at the calcite/quartz boundary serves as a stress concentration point, with limited NaCl precipitation suggesting minimal crystallization impact. Fossils (30%) and open porosity weaken matrix cohesion, but partial pore blockage by weathering products, such as $CaCO_3$, reduces connectivity, mitigating the extent of damage [22].

SEM and EDX analyses of T2 limestone samples (Fig. 14), characterized surface and thin-section morphology and composition, revealing significant alterations following HCl exposure in aqueous conditions. SEM images showed a smoothed, etched appearance with discernible grain boundaries, most evident in (Fig. 16.c). At 376× (20 µm scale), (Fig. 16.d) displayed microscale porosity, rough textures, and prominent cracks, characteristic of carbonate rock weathering, suggesting vulnerabilities to acid infiltration. At 2,14k×25 magnification, (Fig. 16.e) disclosed a highly porous, irregular microstructure with fragmented angular and elongated grains exhibiting sharp, fractured edges, alongside substantial cavities, including a significant void (~30–50 µm) surrounded by smaller pores and grain boundaries. This is indicative of pronounced dissolution and chemical etching. Smooth, rounded surfaces on presumed calcite grains reflect chemical dissolution via the reaction: $CaCO_3(s) + 2HCl(aq) \rightarrow CaCl_2(aq) + H_2O(l) + CO_2(g)$, producing soluble $CaCl_2$, water, and gaseous CO_2. These observations align with recorded losses (ΔM: 1.64%, ΔD: 0.92%, ΔL: 0.66%) post-test, with etching notably intensified in carbonate-rich regions due to calcite's high solubility in acidic environments.

Physico-mechanical properties

The physico-mechanical properties of stones from Tamentfoust fort (T1: PE1-5; T2: PE2-6) were analysed and summarised in Tab. 13. The results revealed that T1 has a low dry density (ρb: 1.68 g/cm³), high porosity (po: 30%), and water absorption (A_b: >3%) (Fig. 17), due to its fossiliferous or micritic limestone composition with calcium carbonate (specific gravity 2.70). As porosity exceeds 15% and capillary absorption (C) reaches 41.58%, T1 is considered unsuitable for structural or wetland applications per ASTM C97/C97M-18 and ISRM standards. T1's compressive strength (σc) is "very low" (po: 4.26 MPa) per ISRM (1972) and ASTM D7012-14 (Fig. 19). This is linked to high calcite content and porosity (>20%) [23], consistent with Norwegian studies correlating strengths below 10 MPa with these traits. In contrast, sample T2, composed of 40% calcite and 35% fossils, displays a moderate density (ρb: 2.22 ± 0.19 g/cm³) and lower porosity (po: 8.59%). XRF analysis, confirming 25% CaO and 5.85% SiO_2, is typical of limestone per ASTM C97 [24]. T2's density is reduced by fossil content and intergranular porosity, partially offset by micritic calcite cement. Iron hydroxides (0.805% Fe) increase microporosity, classifying T2 as "moderately to highly porous" (>5%) per ASTM C97/C642 and NBG (1985) (ASTM C170/C170M Standard Test Method for Compressive Strength of Dimension Stone).

T2's capillary absorption (C) exceeds atmospheric absorption (A_b) (Fig. 17, Fig. 18), indicating interconnected pores and microcracks, worsened by clays (muscovite, chlorite), elongate grains (quartz, plagioclase), and hygroscopic clay properties, raising chemical deterioration risks per ISRM (ASTM C880/C880M Standard Test Method for Flexural Strength of Dimension Stone). Furthermore, T2's uniaxial compressive strength (σ_c: 27.57 ± 0.03 MPa) (Fig. 19) is rated "medium strength" per ISRM, limited by 35% fossils and 0.172% phosphorus as weak points, restricting it to non-load-bearing uses per ASTM C170. T2's flexural strength (σ_f: 1.93 ± 0.03 MPa, maximum 3.73 MPa) falls below the 8 MPa threshold for dimension stone per ASTM C880, driven by its 8.59% porosity and its mineralogical composition: 35% fossils, 0.805% Fe, and clays (1% chlorite, muscovite), with brittle tensile failure resulting from stress concentration at fossil voids and crack propagation.

Non-destructive test results

- Ultrasonic velocity V_p assessment, a key non-destructive testing (NDT) method, was used to evaluate deterioration in the historical building materials of Tamentfoust fort, detecting discontinuities and assessing rock properties. Using a piezoelectric probe, V_p quantifies wave propagation in rocks, reflecting density (ρb), elasticity, porosity (po), and conservation state by measuring travel time (t) and distance between transmitter and receiver. For the T1 limestone sample (PE1-5), the recorded value (V_p: 1.35 km/s) is classified as low, correlating with the uniaxial compressive strength (σ_c: 4.26 MPa), high porosity (po: 30.22%), and moderate density (ρb: 1.68 g/cm³). These values deviate significantly from pure calcite's V_p of 6.49 km/s [25] and typical limestone ranges (5.5–6.5 km/s) per ASTM D2845-08. This aligns with porosity-driven attenuation and σ_c decline, indicating poor cohesion and unsuitability for structural applications per ISRM (1978). In contrast, the T2 sample (PE2-6) exhibits a moderate ultrasonic velocity (V_p: 3.59 ± 0.03 km/s), uniaxial

compressive strength (σ_c: 27.57 MPa), density (ρb: 2.22 g/cm³), and porosity (ρo: 8.59%), consistent with a partially consolidated calcite matrix tempered by fossils and pores. These properties (V_p: 3.5–4.0 km/s; σ_c: 25–40 MPa) indicate medium strength and compactness but fall below optimal limestone standards (4–6 km/s) per ASTM D2845, suggesting limited suitability for deep foundation applications [26].

• The Schmidt hammer rebound test (SHR), a non-destructive method, was used to estimate uniaxial compressive strength (σ_c) by measuring rebound hardness (R), reflecting energy restitution post-impact on stone surfaces. The rebound values were converted to σ_c using rock-specific calibration curves per NF EN 12372, though the method is sensitive to surface roughness, heterogeneity, and moisture. For the T2 limestone sample (PE2-6), a mean R value of 24.28 (minimum 18) was recorded from ten perpendicular rebounds across multiple surface points, ensuring measurement precision per ISRM (1978). Testing of T1 samples was not conducted, as their low uniaxial compressive strength (σ_c: 4.26 MPa) fell outside the recommended 20–150 MPa range per ASTM D5873 and ISRM (1978). Porous or rough surfaces absorb impact energy, reducing the method's reliability for low-cohesion stones like T1, highlighting the influence of intrinsic stone properties on mechanical behaviour. T2's R value corresponds to low-to-moderate compressive strength (20–40 MPa) per ISRM (1981), slightly underestimating the laboratory-measured uniaxial compressive strength (σ_c: 27.57 MPa) due to sclerometer limitations related to surface conditions and microstructure. This moderate strength reflects T2's porous limestone composition, with calcite (40%, Mohs hardness 3) and fossils (35%) limiting durability, while quartz (15%), silica (5.85%), and alumina (1.99%) provide minimal cohesion. Fossil inclusions and variable grain sizes (0.05–3 mm) of quartz and feldspars promote crack propagation under load, despite minor interlocking benefits. Clay minerals (chlorite, muscovite) and iron oxides (0.805%) contribute negligibly to cementation. Porosity (ρo) correlates negatively with SHR and σ_c, while atmospheric water absorption (A_b: 3.31%) and capillary absorption (C: 1.93%) indicate moderate pore connectivity, further reducing mechanical integrity. These properties collectively limit T2's suitability for high-strength applications.

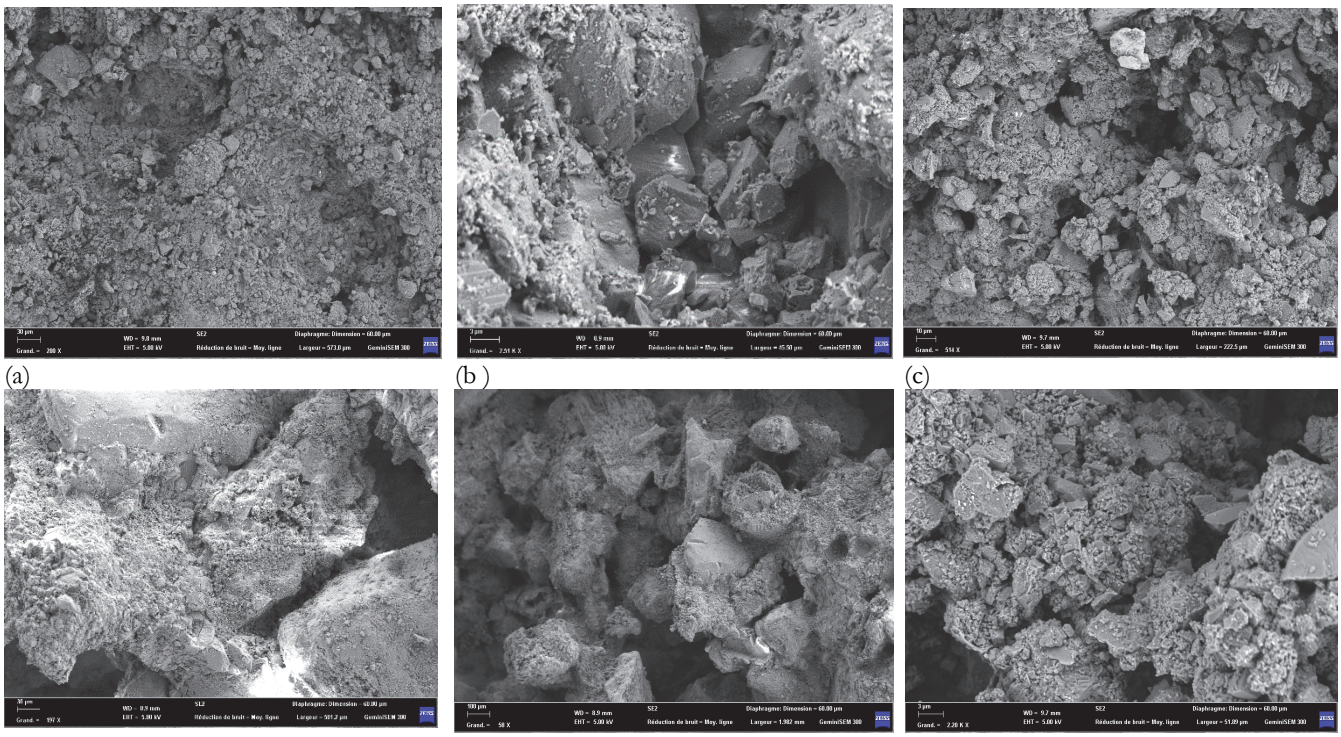

Figure 15: Scanning electron microscopy analysis (SEM) of the T1 stone type, before (a,b,c) and after (d,e,f) salt crystallization test. (a) x200,(b) x2.51k,(c)x514,(d)x197,(e) x58 ,(f)x2.20k.

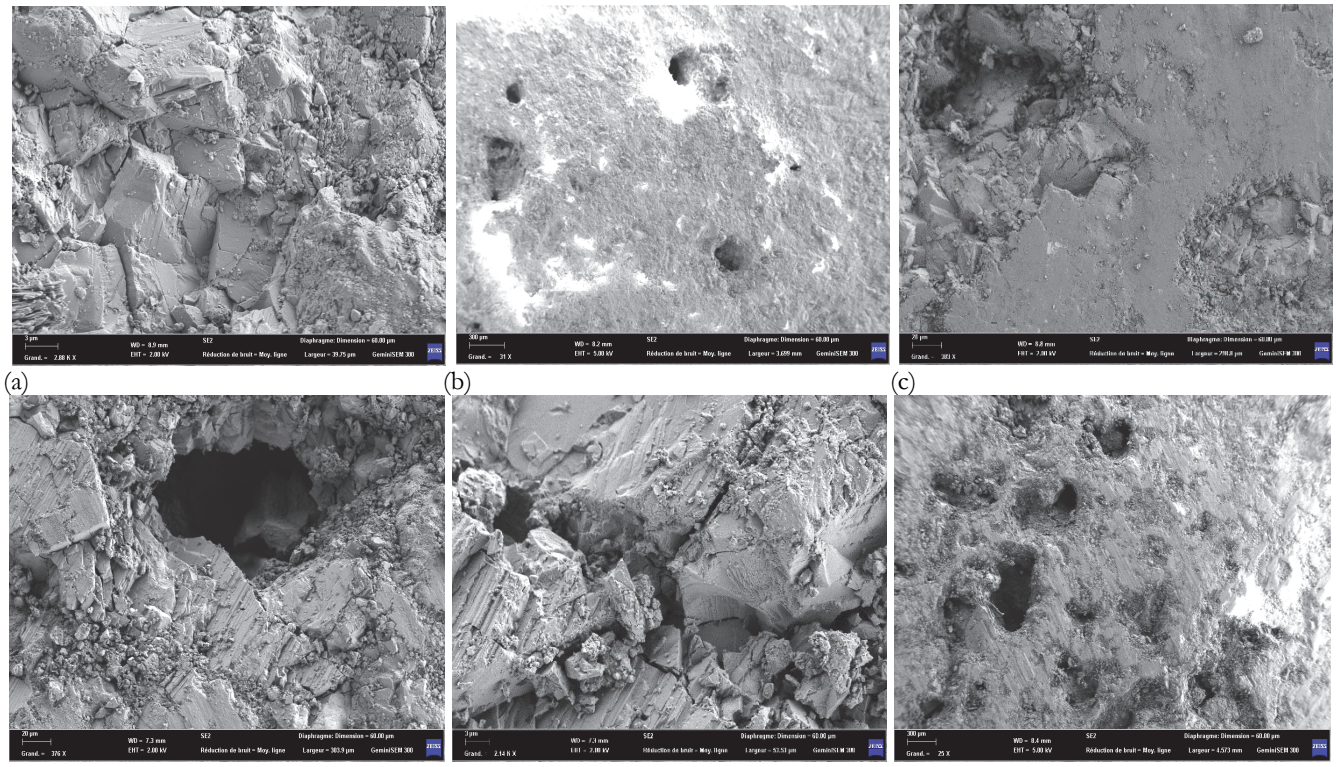

Figure 16: Scanning electron microscopy analysis (SEM) of the T2 stone type, before (a,b,c) and after (d,e,f) ageing test with HCl in the presence of moisture test. (a) x2.88k,(b) x31,(c)x383,(d)x376,(e) x2.14k,(f)x25.

Stone type	Parameter	ρb (g/cm³)	po (%)	A_b (%)	C (g/m². s$^{-½}$)	V_p (km /s)	σ_c (MPa)	R	σ_f (MPa)
T1 1-3	Values	1.68±0.19 n=6	30.22±5.12 n=6	16.08±6.19 n=6	41.58±227.77 n=5	1.35±0.18	4.26±1.93 n=4	-	-
T2 2-4		2.22±0.19 n=3	8.59±1.68 n=3	3.31±0.47 n=3	1.93±12.24 n=3	3.59±0.06	27.57±9.86 n=3	24.28±6.21	3.73±0.42 n=3

$\boldsymbol{\rho b}$ = Density, ***po*** = Porosity, $\mathbf{A_b}$ =Water absorption by atmospheric pressure, $\boldsymbol{C}$= Water absorption by capillarity, $\mathbf{V_p}$= Ultrasonic wave velocity, $\boldsymbol{\sigma_c}$ = Uniaxial compressive strength, **R**= Schmidt hammer rebound strength, $\boldsymbol{\sigma_f}$= flexural strength, **n**= number of the used samples

Table 13: Recap of the physico-mechanical properties of the two stone types T1 and T2.

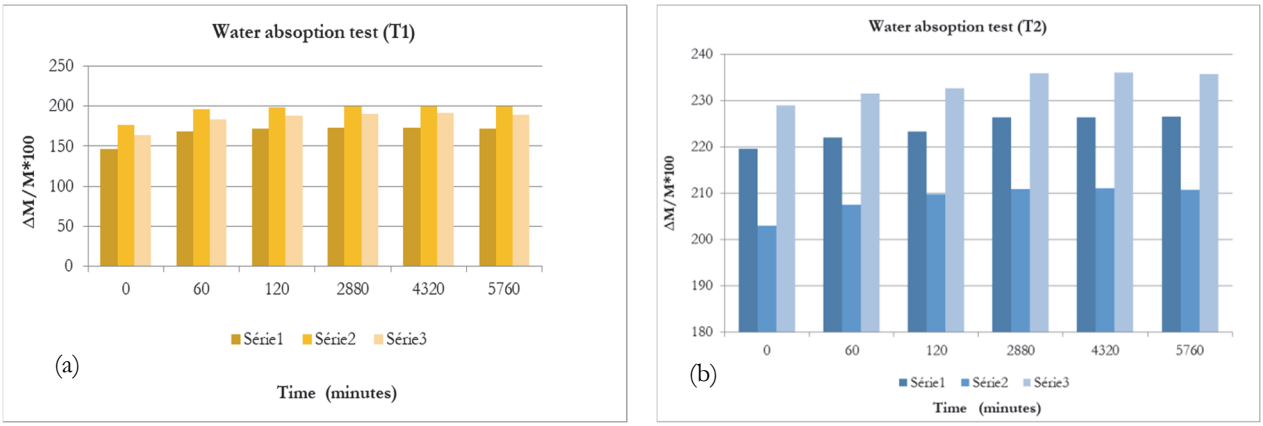

Figure 17: Water absorption: (a) block type T1 (sample PE1-5); (b) block type T2 (sample PE2-6).

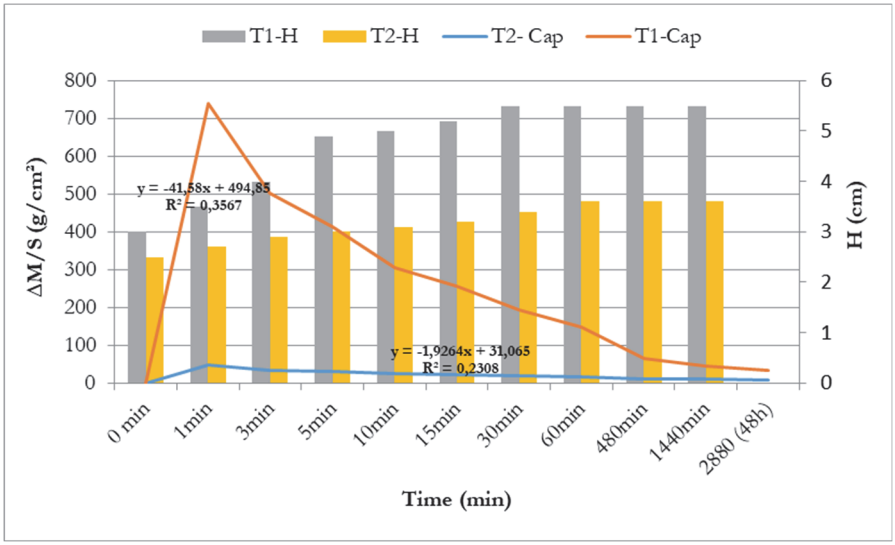

Figure 18: Capillary water absorption, measured as mass uptake per unit area (ΔM/S) and the displacement H of the capillary front along the height of the two types (T1) and (T2) cylindrical sample, in relation to the square root of elapsed time (t).

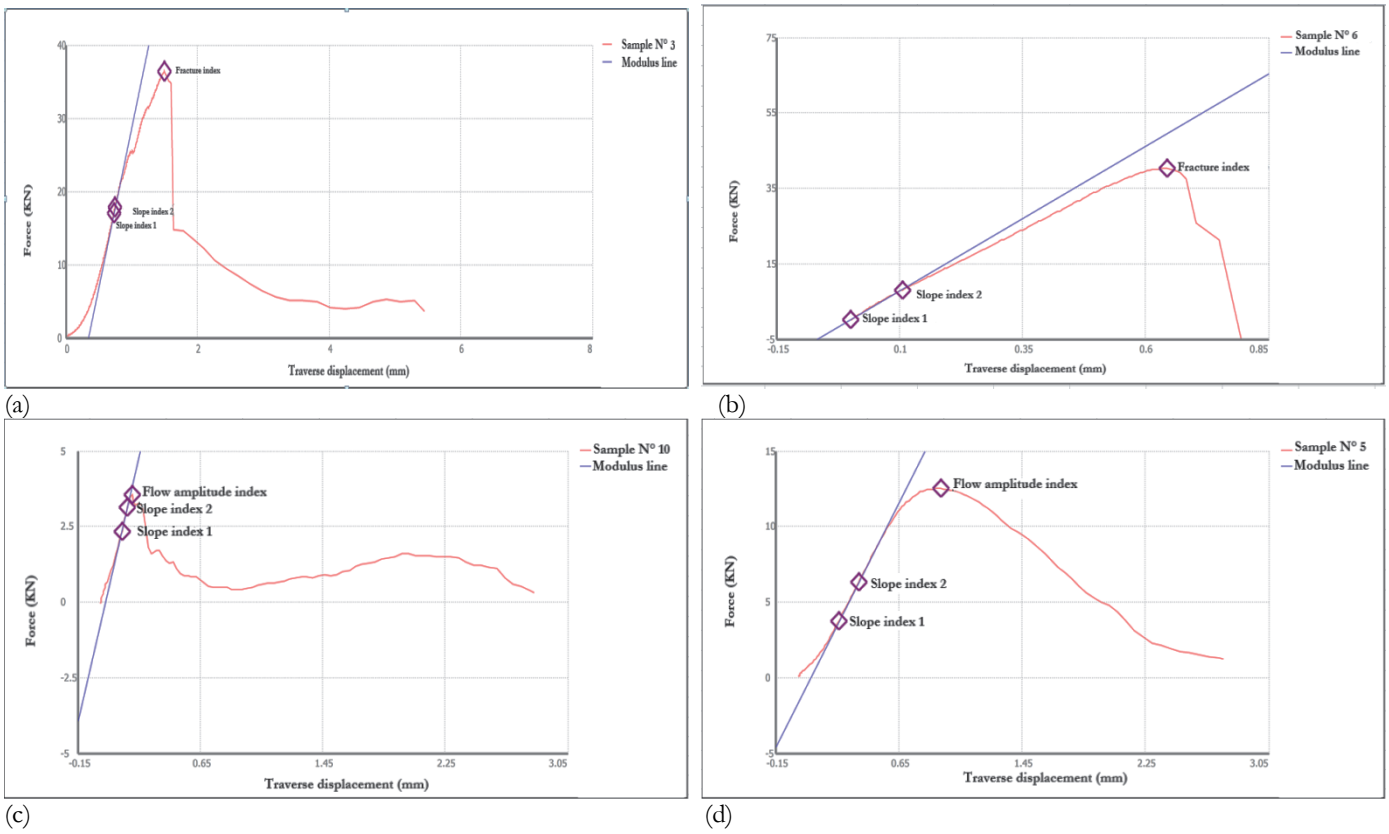

Figure 19: Uniaxial compressive strength test graphic of T1 (a, b) before and after salt crystallization, T2 samples (c, d) before and after ageing test with HCl in the presence of moisture durability tests.

Infrared thermography

Infrared thermography, a non-destructive technique, was applied to evaluate the southern façade of the Tamentfoust heritage building on 19 September, 2024, at 10:15 a.m., capturing surface temperature variations (24.9–33.2°C, mean 28.3–29.9°C) (Fig. 20), to identify degradation patterns, including cracks, moisture, and heat anomalies, influenced by stone emissivity, humidity, and atmospheric conditions. Requiring 1.5–3 hours of solar exposure and an inspection distance of

≤5 m for optimal defect analysis, it outperformed conventional approaches in identifying subsurface issues in historical structures. (Fig. 20.a) (mean 28.3°C) revealed warmer zones (orange/red, ΔT ≈ +3–5°C relative to the mean) on the left side, associated with biological growth forming air pockets that impede heat transfer, contrasting with cooler intact areas (blue/green, ΔT ≈ -1–3°C) indicating moisture retention due to variable stone porosity and capillary water absorption from precipitation or marine spray. Basal deviations suggested vegetation effects.

A horizontal cool transect highlighted fissures and permeable joints, exacerbated by a saline environment promoting salt crystallization and efflorescence, causing mechanical stress. (Fig. 20.b) (mean 29.9°C) showed uniform warmth (orange/yellow, ΔT ≈ +2–3°C), with red zones indicating mortar detachment and honeycombing, and a cooler zone (blue, ΔT ≈ -1–2°C) near joints, reflecting moisture retention in porous and fractured joint materials. (Fig. 20.c) (mean 29.9°C) displayed dispersed cooler zones (ΔT ≈ -1–3°C) across the stone, suggesting moisture pockets from internal fissures and delamination driven by non-uniform weathering and mineral variability.

Saline conditions at Tamentfoust fort exacerbated deterioration through salt crystallization within pores and fractures, amplifying efflorescence and mechanical damage. Small-scale thermal variations, detected via infrared thermography indicated alveolarization, though results were moderated by resolution limits and environmental factors. Key degradation mechanisms include excessive moisture infiltration through joints, fissures, and the stone matrix, compounded by variable porosity. These conditions heighten risks of internal fractures, surface delamination, and joint degradation, further aggravated by saline-induced salt crystallization, which causes both mechanical and chemical damage to the stone structure.

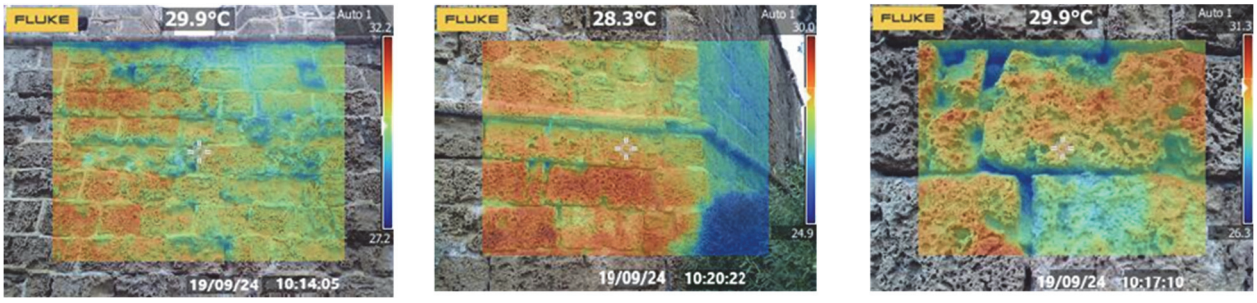

(a) (b) (c)

Figure 20: Thermographic images of the southern fort façade.

Durability tests

Two durability tests were conducted on stone samples from Tamentfoust fort to assess material responses to physical-mechanical stress and environmental degradation. The first test evaluated the salt crystallization resistance of T1 limestone samples, following standardized procedures (Fig. 21). The second test assessed resistance to accelerated aging in an acidic environment using hydrochloric acid (HCl) and moisture, conducted on T2 limestone samples. Both tests employed visual examination, uniaxial compressive strength (σ_c), dry weight, and dimensional loss metrics. Analytical techniques, including crackmeter microscopy (Fig. 22), SEM-EDX (Fig. 15), petrographic analysis (Fig. 9), XRD, and XRF (Fig. 13), were used to characterize pre- and post-test alterations Tab. 8.

Physical changes

Soluble salts, alongside water, are primary agents of stone deterioration, causing crystallization stresses that exceed tensile strength, reducing it to powder, and micro-cracking. These salts, sourced from marine aerosols and pollution, contribute to hydration-related damage through multi-state salt transformations. Salt crystallization tests on cylindrical stone samples, conducted over 15 cycles, revealed a mean MDL-Loss (mass loss of ΔM: 0.65%, <1%) Tab. 14, after an initial slight mass increase likely due to halite growth in pores >1 μm, indicating low susceptibility to salt weathering, classifying the stone as durable per ISRM and ASTM C88 standards. Mass loss (ΔM), accelerated between cycles 5–10 due to mechanical disintegration from salt-induced pore stresses, caused spalling and micro-cracking (Fig. 19). A non-linear diameter reduction (ΔD) exhibited cycle-dependent acceleration, reflecting anisotropic deformation tied to crystal orientation and stone heterogeneity, while a minor length reduction (ΔL), less pronounced than diameter loss, suggested axis-dependent mechanical strength influenced by porosity and crack propagation. Crystal expansion within pores drove cracking and structural weakening, with pore size correlating to crystallization pressure, yielding significant transverse dimension loss

(Fig. 22). Weight loss exceeded dimensional changes, indicating internal disintegration from cumulative salt-induced fatigue before visible alteration Tab. 14**.**

Consequently, severe damage emerged during wetting phases post-drying crystallization, reducing uniaxial compressive strength (σ_c) to 4.01 MPa. Moderate porosity facilitated salt infiltration without significant degradation, aligning with durable limestone characteristics in harsh freeze-thaw conditions per ASTM C97/C97M-18, ISRM (Suggested Methods for Porosity Characterisation), and ASTM C97/C97M-18 (Test Methods for Absorption and Bulk Specific Gravity of Dimension Stone).

Salt crystallization tests on T1 limestone samples from Tamentfoust fort, using NaCl salt dissolution per EN 12370, revealed a modest mass loss (ΔM: 0.65%) after 10 cycles, indicating exceptional durability despite progressive damage, as assessed by ASTM C97/C97M-18 [27]. High-temperature drying (105°C) accelerated degradation beyond natural conditions, amplifying microcracking under crystallization pressures of 10–20 MPa. The stone's mineralogical composition, comprising 50% calcite, 30% fossils (prone to dissolution), alongside durable 14% quartz and feldspars (plagioclase, microcline), contributes to mass loss through dissolution and fragmentation of components, amplified with each cycle (Fig. 13).

(a) (b) (c) (d) (e) (f)

Figure 21: Durability Assessment of stone sample type T1: determination of resistance by salt crystallization test & microscopic view under the crackmeter microscope. (a) PE1-5 sample before test, (b, c) PE1-3 sample after test, (d) PE1-3 sample uniaxial compressive strength assessment after the test. (e, f) respectively, microscopic view of PE1-5, PE1-3 before after salt crystallization test.

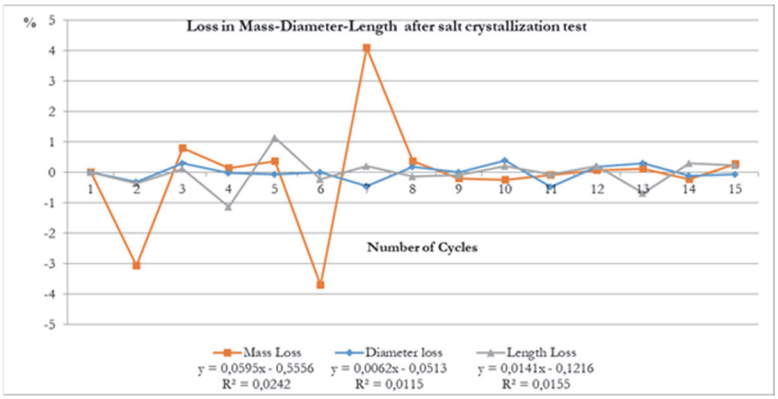

Figure 22: Loss in mass, diameter and length after salt crystallization of the T1 type block sample.

Stone type	Parameter	σ_c (MPa)	$\sigma_{c-\Delta f}$ (MPa)	MDL-Loss %		
				ΔM	ΔD	ΔL
T1 1-3	Values	4.26±1.93	4.01±2.61	0.65	0.18	0.03

(σ_c): Uniaxial compressive strength before the test, ($\sigma_{c-\Delta f}$): Uniaxial compressive strength after the test, **(**M):loss in mass, (D) loss in diameter dimension,(L) loss in length.

Table 14: PE1-3 sample assessment results after salt crystallization test.

Extensive research on the impact of anthropogenic pollutant emissions on historic limestone buildings and monuments reveals multiple deterioration mechanisms, including cracking, splitting, spalling, softening, and staining, driven by salt and water crystallization processes and acid-base chemical dissolution reactions (Fig. 23). Accelerated laboratory testing using hydrochloric acid (HCl) effectively simulates outdoor degradation patterns, providing a rapid and quantifiable assessment of limestone deterioration within practical timeframes. HCl, a highly reactive atmospheric gas, is efficiently removed near emission sources through interactions with cloud water and surfaces, with NH_4Cl aerosols or particles serving as a key environmental sink, governed by the reversible reaction: $NH_4Cl(s) \rightarrow HCl(g) + NH_3(g)$. Research on limestone deterioration highlights that the humidity-dependent equilibrium of NH_4Cl, stable above 10°C only with elevated HCl and NH_3 concentrations, regulates atmospheric HCl levels, with stability increasing at lower temperatures. Despite limestone's varied appearance and durability due to diverse geological origins, deterioration mechanisms, including cracking, spalling, and chemical dissolution, remain consistent. Acid gas-induced degradation, particularly from HCl in air pollution, is slower and less perceptible than rapid salt crystallization decay but is a critical weathering agent, notably promoting kaolinization of feldspar minerals into kaolinite through chemical reactions:

$$2KAlSi_3O_8 + 2H_2CO_3 + 9H_2O \rightarrow Al_2Si_2O_5(OH)_4 + 4H_4SiO_4 + 2K^+ + 2HCO_3^-$$

underscoring its role in gradual but significant structural alteration. This reaction shows how feldspar ($KAlSi_3O_8$) reacts with carbonic acid (H_2CO_3) and water to form kaolinite ($Al_2Si_2O_5(OH)_4$), silicic acid (H_4SiO_4), potassium ions (K^+), and bicarbonate ions (HCO_3^-).

Exposure to gaseous HCl induced physical and mechanical alterations in T2 limestone samples PE2-4 from Tamentfoust fort, resulting in a mass loss (ΔM: 1.64%), length reduction (ΔL: 0.66%), and diameter reduction (ΔD: 0.92%), indicating high durability per ASTM C88 (<2% mass loss), ASTM D5240 (<5%), and ISRM (2007) (<3%) Standards for Acid-Exposed Structural Rocks Tab. 15. Low-to-moderate porosity (*Po*: 1–5%, per ASTM C97) limits HCl infiltration, reducing calcite dissolution and maintaining mass loss (ΔM) below 2%, consistent with dense, low-porosity limestones (1–2% mass loss). Dimensional losses (average 0.79%, <2% per ASTM D5240, <1% per ISRM) reflect mechanical stability, with a slight diameter bias (ΔD: 0.92% vs. ΔL: 0.66%) likely due to radial HCl diffusion and crystal orientation in an anisotropic matrix (Fig. 24). HCl exposure reduced uniaxial compressive strength (σ_c) from 27.57 MPa to 17.94 MPa (~35% decline) (Fig. 19), linked to mass losses of 1.8% (sample E2.1) and 3% (sample E2.3) and dimensional reductions (diameter: 0.8–1%, length: 1–1.5%), with a 1–2% mass loss (ΔM) typically lowering strength by 5–10%, deemed acceptable for construction per ASTM C1524. Calcite dissolution, the primary binder, increases porosity (*po*), generating microcracks via differential dissolution, $CaCl_2$ crystallization, and CO_2 release, weakening intergranular bonds despite 15% quartz resistance. A 10% porosity increase can reduce strength by 20–40% by creating stress foci (Griffith's theory), exacerbated by microstructural changes, such as roughened surfaces and stiffness gradients from selective calcite loss and cyclic $CaCl_2$-driven dissolution-crystallization. Local heterogeneity in porosity and mineral distribution explains sample variations (E2.1: 1.8% mass loss; E2.3: 3% mass loss), indicating moderate acid sensitivity and necessitating cautious use in acidic environments, such as urban pollution settings, with ISRM (2015) recommending further freeze-thaw testing.

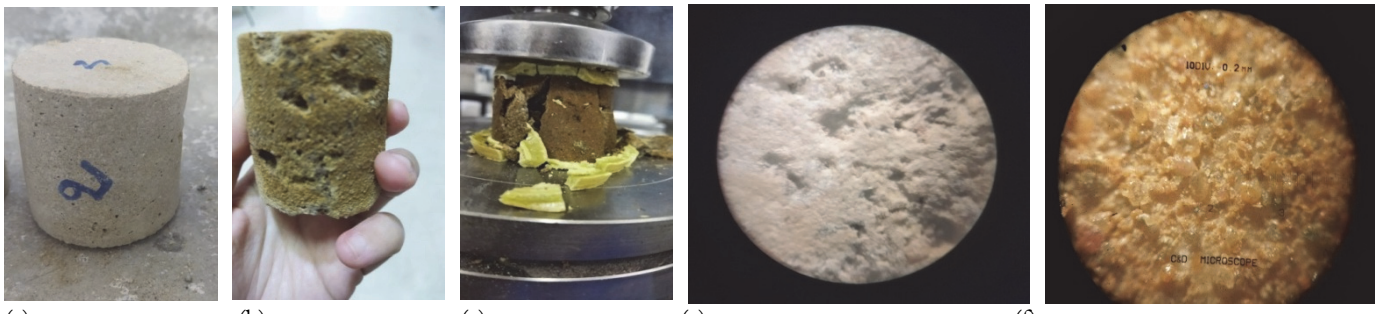

(a) (b) (c) (e) (f)

Figure 23: Durability assessment of stone sample type T2: determination of resistance to accelerated ageing with HCl in the presence of moisture & microscopic view under the crackmeter microscope. (a) PE2-6 sample before test, (b, c) PE2-4 sample after test, (d) PE2-4 sample uniaxial compressive strength assessment after the test. (e, f) respectively, microscopic view of PE2-6, PE2-4 before and after ageing test.

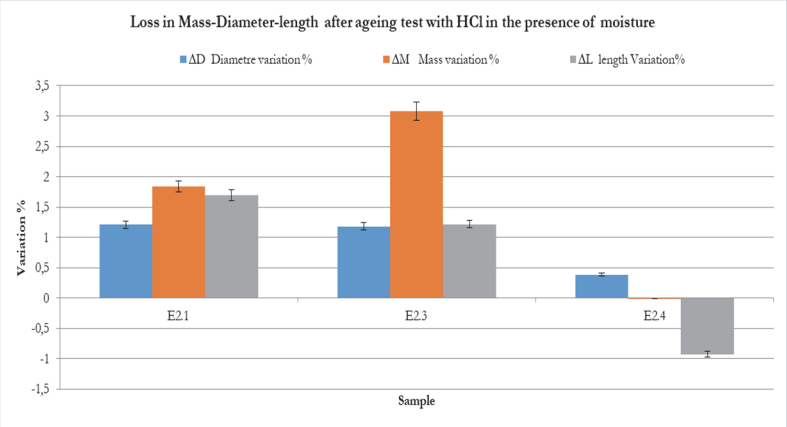

Figure 24: Loss in mass, diameter and length after ageing test with HCl in the presence of moisture.

Stone type	Parameter	σ_c (MPa)	σ_{c-Af} (MPa)	MDL-loss %		
				ΔM	ΔD	ΔL
T2 1-3-4	Values	27.57 ±9.86	17.94 ±0.78	1.64	0.92	0.66

(σ_c): Uniaxial compressive strength before the test, (σ_{c-Af}): Uniaxial compressive strength after the test, **(**M):loss in mass, (D) loss in diameter dimension,(L) loss in length.

Table 15: PE2-4 sample assessment results after ageing test with HCl in the presence of moisture.

The structure's apparent degradation

A terrestrial laser scanning (TLS) 3D survey of Tamentfoust fort façades, documented in (Fig. 25), revealed extensive pathological features, including widespread cracking and rendering mortar detachment across all sections, notably at corners, cornices, and basements. Mould on upper interior façade coatings suggests water infiltration, fostering humidity and biofilm formation from rainwater. External upper façades exhibit prevalent biological growth. The south façade, constructed of porous, soft limestone blocks (light beige to brownish), is most severely affected due to solar radiation, which exacerbates coating humidity and dust accumulation, as it faces the sea and the town's port. Despite regular block cuts and defined joints, irregular joint widening reflects mortar degradation and erosion. Southern exposure drives significant thermal fluctuations, compounded by driving rain and abrasive winds, with vegetation in joints and blocks, alongside dark stains and whitish deposits, indicating moisture retention and active chemical-biological degradation.

Detailed identification of degradation types

The south façade exhibits extensive degradation, characterized by multiple mechanisms (Fig. 26). Efflorescence, manifesting as whitish deposits from salt crystallization (chlorides from marine air, sulphates from mortar or pollutants), is prominent in central and upper blocks, intensified by capillary rise and rapid evaporation, which promote subflorescence and disintegration. Disintegration, observed as granular fragmentation in mid-height and lower blocks, results from wetting-drying cycles, thermal stress, and low stone resilience, worsened by efflorescence and biological colonization. Vegetation (mosses, higher plants) in joints and blocks, alongside dark microbial stains, indicates moisture retention and acid-induced mineral dissolution, amplifying cracking. White, web-like patches, likely spider webs or salt efflorescence (possibly with calcium carbonate deposits), reflect coastal influences and high porosity. Micro-cracks, predominantly near colonized areas, arise from thermal expansion, root pressure, and salt crystallization, facilitating further water ingress. Erosion, marked by smoothed upper blocks and alveolar cavities, results from runoff and wind, exacerbated by disintegration. Staining (brownish, dark) from pollution, chemical reactions, or lichens, along with gypsum crusts, adds subsurface pressure.

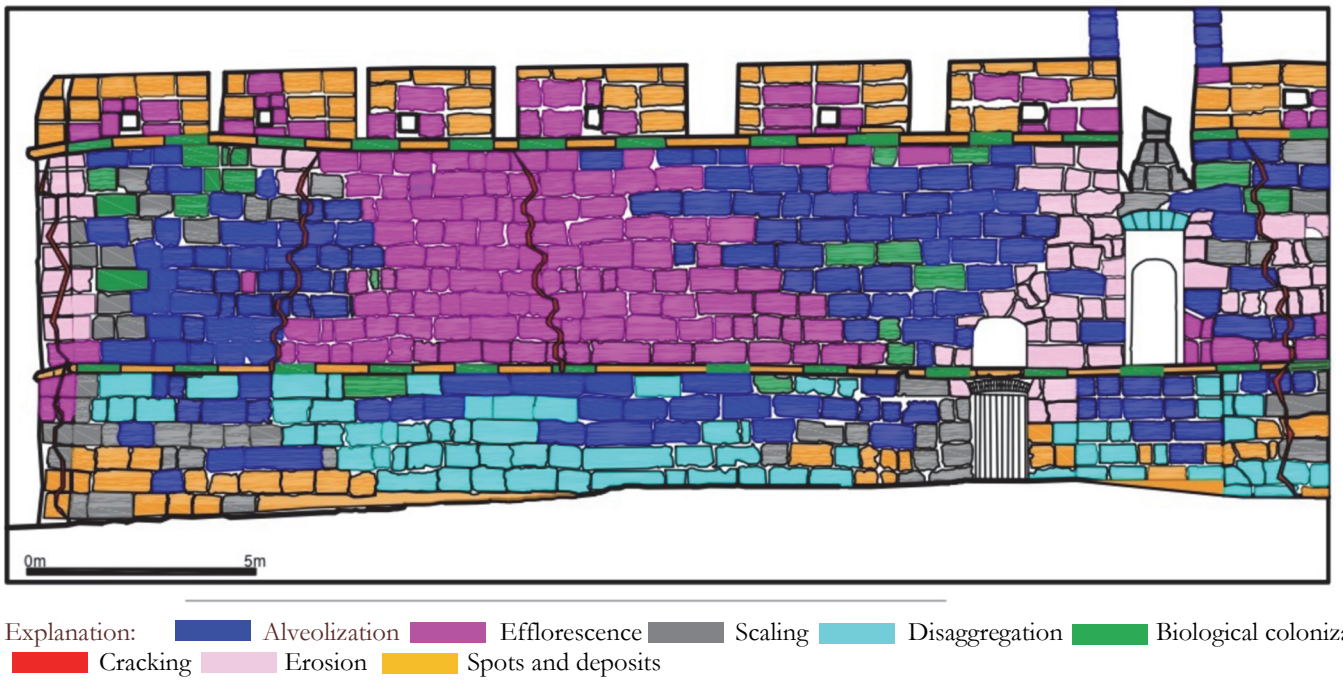

Figure 25: Deterioration mapping of the southeast fort façade.

Mapping and quantitative analysis

Quantitative analysis assesses façade deterioration through affected surface area (Fig. 25), spatial distribution, and severity, employing indices (mild, moderate, severe) based on visual and measured criteria [28].

Efflorescence, covering ~15% of the façade (~40% of central-upper blocks, ~70% of total affected area), manifests as moderate whitish deposits, concentrated in sun-exposed central-right and upper zones, due to rapid evaporation. Disintegration affects ~15% of the surface (~50% of central blocks, ~30% of lower blocks, ~50% of total affected façade), ranging from moderate to severe, with friable, cavity-ridden textures prominent in moisture-retaining central-lower regions. Biological colonization impacts ~5% of the surface (~10% higher plants in left-central joints and blocks, ~5% lichen/algae stains, right-side dominant), rated moderate, reflecting advanced but limited rooting and superficial staining. Cracking, affecting ~10% of the façade surface, manifests as micro-cracks (~5% of blocks, left-central) and degraded joints (~5–10%), with mild-to-moderate severity indicating superficial damage and early structural cracking near biologically colonized zones due to root pressure. Erosion, spanning ~10% of the surface (~30% of upper blocks, ~10% of central blocks), rated moderate, with smoothed surfaces and material loss concentrated in runoff-exposed upper and disintegration-prone central areas.

Staining/soiling covers ~10% of the façade, including non-biological dark and brownish stains of mild-to-moderate severity, predominantly in right-upper regions, likely from windborne pollutants, distinct from lichen-related marks. Alveolization, covering ~20% of the façade, manifests as severe damage, concentrated in upper-right and left zones, primarily attributed to saline crystallization (NaCl, $CaCl_2$) induced by the marine environment, exacerbated by variable porosity and chemical dissolution of calcite by chloride ions. Solar radiation accelerates wet-dry cycles, intensifying thermal and mechanical stresses. High-porosity zones (fossils, microfissures) and permeable joints are particularly susceptible. Tab. 16 summarizes the weathering types of Tamentfoust fort facade.

Figure 26: Southern fort façade type of damage (a) biological colonization, (b) scaling, (c) alveolization, (d) disaggregation and lichen colonization, (e) special biological colonization by a spider web, (f) erosion, (g)cracking, (h) black crust ,(i) effloresce.

Type of damage	Percentage of total area (%)	Severity	Spatial distribution
Efflorescence	15	Moderate	Central-right, upper
Scaling	15	Severe	Right and left corners
Alveolization	20	Severe	Upper, central
Disaggregation :Powdering, Crumbling	15	Moderate to severe	Central, lower
Biological colonisation	05	Moderate	Left, central (plants); right (spots)
Cracking (Fracture, hair crack, craquelet)	10	Slight to moderate	Left, central (near vegetation)
Erosion	10	Moderate	Upper, central
Spots and deposits (salt crust, black crust)	10	Slight to moderate	Right, upper

Table 16: Type of damage on the southeast fort façade.

CONCLUSION

This study investigates limestone deterioration in Tamentfoust fort, a historical structure, using both destructive (DT) and non-destructive (NDT) testing methods to assess material degradation and inform restoration strategies. Two distinct limestone types (T1 and T2) were identified, differing significantly in mineralogical, chemical, and physico-mechanical properties. T1, characterized by high porosity (*po*: >30%), moderate density (*ρb*: 1.68 g/cm³), and calcite dominance (50%), exhibits low ultrasonic velocity (V_p: 1.35 km/s) and a mean uniaxial compressive strength (σ_c: 4.26 MPa), reflecting a brittle microstructure with fossils (28%) and interconnected pores that enhance water absorption (A_b) and susceptibility to degradation. In contrast, T2 displays moderate to high ultrasonic velocity V_p, higher compressive strength (σ_c: 27.57 MPa), and lower porosity (*po*: <10%), indicating greater compactness. Durability tests, including HCl exposure and NaCl crystallization, reveal T1's vulnerability to calcite dissolution, increasing porosity and reducing strength by 35% (from 27.57 MPa to 17.94 MPa), with mass loss (ΔM: 1.64%) and microcrack formation observed via SEM. T2 demonstrates better resistance, though fossils and porosity (*po*: 8.59%) still limit flexural strength (σ_f: 3.73 MPa). Salt crystallization induces damage through pore wall stress, particularly in microporous structures, aligning with crystal bridging theory. XRF and EDX analyses highlight calcite dissolution and salt accumulation, exacerbating degradation in saline and acidic conditions. Furthermore, thermal imaging indicates surface temperature variations (24.9–33.2°C), influenced by capillary absorption (*C*) and environmental factors. These findings underscore the role of porosity and mineralogy in limestone durability, suggesting protective measures for preservation in acidic and saline environments using a multidisciplinary approach in the characterisation of construction materials. To mitigate deterioration, we recommend some solutions which we classified as follow:

Restoration strategies:

- Protective coatings and consolidants: Given T1's high porosity and susceptibility to water absorption and salt crystallization, recommend the application of hydrophobic coatings or consolidants (e.g., silane-based treatments or calcium hydroxide-based nano-lime) to reduce water ingress and enhance resistance to chemical weathering. These treatments can stabilize the porous microstructure and mitigate calcite dissolution in acidic environments.
- Targeted repair for T1 limestone: Since T1 exhibits low compressive strength and significant deterioration (35% strength reduction), propose selective replacement of severely degraded T1 blocks with compatible limestone matching T2's properties (lower porosity, higher strength) to ensure structural integrity while preserving historical authenticity.
- Salt removal techniques: To address salt accumulation (NaCl crystallization), suggest desalination methods such as poulticing with clay-based materials or controlled washing to remove soluble salts from T1's microporous structure, reducing pore wall stress and microcrack formation.

Preventive measures for long-term preservation:

- Environmental Control: Since thermal imaging revealed surface temperature variations (24.9–33.2°C) linked to capillary absorption, recommend environmental management strategies, such as improved drainage systems around the fort to minimize moisture infiltration and capillary rise, which exacerbate salt and acid damage.
- Periodic monitoring: Propose a routine structural health monitoring (SHM) program using non-destructive techniques (e.g., ultrasonic testing, thermal imaging) to track ongoing deterioration, particularly in T1 zones, and detect early signs of microcracking or salt-induced damage [29].

Integration of Advanced Technologies:

- Machine learning and multiscale diagnostics: Expand on the mention of machine learning (ML) by specifying how it can be applied. For instance, ML algorithms could be trained on ultrasonic velocity (Vp), porosity (po), and SEM data to predict degradation patterns and prioritize restoration zones. Propose developing a predictive model to correlate environmental factors (e.g., humidity, salinity) with material decay rates.
- Composite durability index: Elaborate on the proposed composite index by outlining its potential components, such as porosity, compressive strength, and salt crystallization resistance, weighted based on their impact on durability. Suggest pilot testing this index using data from T1 and T2 to validate its efficacy in assessing limestone condition.
- Digital twin technology: Recommend creating a digital twin of the fort, integrating NDT and DT data with real-time SHM inputs, to simulate deterioration scenarios and optimize restoration strategies under varying environmental conditions.

Material Compatibility and Sourcing:

- Local material sourcing: To ensure compatibility with the original limestone, propose geological surveys to identify local quarries with limestone matching T2's mineralogical and mechanical properties (e.g., calcite content >50%, porosity <10%, σc ~27 MPa). This ensures sustainable and historically appropriate restoration.
- Laboratory testing of replacement materials: Suggest conducting accelerated weathering tests (e.g., NaCl crystallization, HCl exposure) on potential replacement materials to confirm their durability in the fort's saline and acidic environment before use.

ACKNOWLEDGMENTS

The authors express their gratitude to Yanis SIBACHIR for his significant and substantial contribution to the realization of the 3D simulation using a laser scanner 3D, for the survey of the Ottoman fort The authors would like to thank Dr. Nora KHOUAL , for her valuable support in the experimental tests and data analysis. Additionally, they are also grateful to Dr. Rachid AMOKRANE for granting access to laboratory testing facilities. A special recognition goes to Mrs. Razika FERHI and her laboratory team, for her precious help in the experimental testing and data assessment.

REFERENCES

[1] Keshmiry, A., Hassani, S., Dackermann, U., Li, J. (2024). Assessment, repair, and retrofitting of masonry structures: A comprehensive review, Constr. Build. Mater., 442, pp. 137380, DOI: https://doi.org/ 10.1016/J.CONBUILDMAT.2024.137380.

[2] Antonelli, F., Savalli, A., Cantisani, E., Fratini, F., Giamello, M., Lezzerini, M., Pecchioni, E., Tesser, E. (2016). Multianalytical approach to diagnosis and conservation of building materials: the case of Punta Troia Castle in Marettimo (Aegadian Islands—Sicily, Italy), Appl. Phys. A Mater. Sci. Process., 122(4), pp. 1–10, DOI: https://doi.org/ 10.1007/S00339-016-9803-6.

[3] Tesser, E., Lazzarini, L., Ganzerla, R., Antonelli, F. (2017). The decay of the polysiloxane resin Sogesil XR893 applied in the past century for consolidating monumental marble surfaces, J. Cult. Herit., 27, pp. 107–115, DOI: https://doi.org/ 10.1016/J.CULHER.2017.03.001.

[4] Mahindad, N.A. (2020). Influence of natural additives and crushed bricks on the physical and mechanical properties of repair and restoration mortars, Int. J. Phys. Sci., 15(2), pp. 60–69, DOI: https://doi.org/ 10.5897/IJPS2020.4867.

[5] Ouagueni, Y. (2008).1. In: Casanovas, X., (Ed.), Réhabilitation et revitalisation urbaine à Oran, Barcelona,Spain, p. 143.

[6] Espinoza, W.F., Moposita, R., Torres, A., Moro, C. (2025). Characterizing marble strength and elasticity: Insights from destructive and non-destructive techniques on El Laurel formation (Ecuador), Constr. Build. Mater., 468, pp. 140340, DOI: https://doi.org/ 10.1016/J.CONBUILDMAT.2025.140340.

[7] Izzo, F., Furno, A., Cilenti, F., Germinario, C., Gorrasi, M., Mercurio, M., Langella, A., Grifa, C. (2020). The domus domini imperatoris Apicii built by Frederick II along the Ancient Via Appia (southern Italy): An example of damage diagnosis for a Medieval monument in rural environment, Constr. Build. Mater., 259, pp. 119718. DOI: https://doi.org/ 10.1016/J.CONBUILDMAT.2020.119718,

[8] Rossi, M., & Bournas, D. (2023). Structural health monitoring and management of cultural heritage structures: a state-of-the-art review, Appl. Sci., 13(11), DOI: https://doi.org/ 10.3390/app13116450.

[9] Fehér, K., Török, Á. (2022). Detecting short-term weathering of stone monuments by 3D laser scanning: lithology, wall orientation, material loss, J. Cult. Herit., 58, pp. 245–255, DOI: https://doi.org/ 10.1016/J.CULHER.2022.10.012.

[10] Gsell, S. (1973). Atlas archéologique de l'Algérie, Paris, O.Zeller.

[11] Salama, P. (1999). Chronique d'une ville disparue: Rusguniae de Maurétanie Césarienne, Bull. La Société Natl. Des Antiq. Fr., 1996(1), pp. 129–143, DOI: https://doi.org/ 10.3406/BSNAF.1999.11285.

[12] Glangeaud.L. (1932). Etude géologique de la région littorale de la Province d'Alger, 2, pp. 350–598.

[13] Rabahi Touloum, N., Brara, A. (2023). Advanced decay of the Fontvieille porous limestone used in the construction of Pouillon's housing estates in Algiers (Algeria), J. Archaeol. Sci. Reports, 47, pp. 103804, DOI: https://doi.org/ 10.1016/J.JASREP.2022.103804.

[14] Alves, C., Figueiredo, C., Maurício, A., Aires-Barros, L. (2017). Salt weathering of natural stone: A review of the influence of stone properties on salt weathering mechanisms and implications for conservation. , Environ. Earth Sci., 76(12), pp. 1–15.
[15] Belhout, D., Kerbachi, R., Relvas, H., Miranda, A.I. (2018). Air quality assessment in Algiers city, Air Qual. Atmos. Heal., 11(8), pp. 897–906, DOI: https://doi.org/ 10.1007/S11869-018-0589-X.
[16] La Russa, M.F., Fermo, P., Comite, V., Belfiore, C.M., Barca, D., Cerioni, A., De Santis, M., Barbagallo, L.F., Ricca, M., Ruffolo, S.A. (2017). The Oceanus statue of the Fontana di Trevi (Rome): The analysis of black crust as a tool to investigate the urban air pollution and its impact on the stone degradation, Sci. Total Environ., 593–594, pp. 297–309, DOI: https://doi.org/ 10.1016/J.SCITOTENV.2017.03.185.
[17] Dimitraki, L., Devlioti, K., Christaras, B., Arampelos, N., Chatziangelou, M. (2018). The P-Wave Ultrasonic Velocity and Infrared Thermometer Nondestructive Techniques for Estimating the Surface Weathering and the Depth of the Consolidation Liquid on Historical Monuments, 10th Int. Symp. Conserv. Monum. Mediterr. Basin, pp. 243–50, DOI: https://doi.org/ 10.1007/978-3-319-78093-1_24.
[18] Solla, M., Maté-González, M.Á., Blázquez, C.S., Lagüela-López, S., Nieto, I.M. (2024). Analysis of structural integrity through the combination of non-destructive testing techniques in heritage inspections: The study case of San Segundo's hermitage (Ávila, Spain), J. Build. Eng., 89, pp. 109295, DOI: https://doi.org/ 10.1016/J.JOBE.2024.109295.
[19] Fitzner, B., Heinrichs, K. (2002).Damage diagnosis on stone monuments – weathering forms, damage categories and damage indices. Acta Universitatis Carolinae Geologica, 45, pp. 12–13.
[20] Liu, S., Bin Mamat, M.J. (2024). Application of 3D laser scanning technology for mapping and accuracy assessment of the point cloud model for the Great Achievement Palace heritage building, Herit. Sci., 12(1), pp. 1–17, DOI: https://doi.org/ 10.1186/s40494-024-01252-y.
[21] Nesse, W.D. (2024). Introduction to mineralogy, , pp. 539.
[22] Granneman, S.J.C., Lubelli, B., van Hees, R.P.J. (2019). Effect of mixed in crystallization modifiers on the resistance of lime mortar against NaCl and Na2SO4 crystallization, Constr. Build. Mater., 194, pp. 62–70, DOI: https://doi.org/ 10.1016/J.CONBUILDMAT.2018.11.006.
[23] Belfiore, C.M., Calabrò, C., Ruffolo, S.A., Ricca, M., Török., Pezzino, A., La Russa, M.F. (2021). The susceptibility to degradation of stone materials used in the built heritage of the Ortygia island (Syracuse, Italy): A laboratory study, Int. J. Rock Mech. Min. Sci., 146, pp. 104877, DOI: https://doi.org/ 10.1016/J.IJRMMS.2021.104877.
[24] Folk, R.L. (1962).Spectral subdivision of limestone types. In: Memoir of the American Association of Petroleum Geologists, (Ed.), Classification of carbonate rocks , vol. volume I, William E. Ham, Tulsa Oklahoma, pp. 62–84.
[25] Shaeri, J., Mahdavinejad, M., Zalooli, A. (2022). Physico-mechanical and Chemical Properties of Coquina Stone Used as Heritage Building Stone in Bushehr, Iran, Geoheritage, 14(3), pp. 1–11, DOI: https://doi.org/ 10.1007/s12371-022-00738-0.
[26] Benavente, D., Cueto, N., Martínez-Martínez, J., García Del Cura, M.A., Cañaveras, J.C. (2007). The influence of petrophysical properties on the salt weathering of porous building rocks, Environ. Geol., 52(2), pp. 197–206, DOI: https://doi.org/ 10.1007/S00254-006-0475-Y.
[27] Godts, S., Orr, S.A., Steiger, M., Stahlbuhk, A., De Kock, T., Desarnaud, J., De Clercq, H., Cnudde, V. (2023). Salt mixtures in stone weathering, Sci. Rep., 13(1), pp. 1–10, DOI: https://doi.org/ 10.1038/s41598-023-40590-y.
[28] Piovesan, R., Tesser, E., Maritan, L., Zaccariello, G., Mazzoli, C., Antonelli, F. (2023). Mapping of stones and their deterioration forms: the Clock Tower, Venice (Italy), Herit. Sci., 11(1), pp. 1–27, DOI: https://doi.org/ 10.1186/s40494-023-00909-4.
[29] Khatir, A., Capozucca, R., Khatir, S., Magagnini, E., Le Thanh, C., Riahi, M.K. (2025). Advancements and emerging trends in integrating machine learning and deep learning for SHM in mechanical and civil engineering: a comprehensive review, J. Brazilian Soc. Mech. Sci. Eng., 47(9), pp. 1–34, DOI: https://doi.org/ 10.1007/S40430-025-05697-5.

LIST OF ABBREVIATIONS

Abbreviation	Definition	Abbreviation	DefinitionSignification
DT	Destructive Technique	A_b	water absorption by atmospheric pressure in %
EDX	Energy Dispersive Spectroscopy	C	Capillary water absorption in (g/m2/s ^0.5)
ICDD	International Centre for Diffraction Data	M_d	Mass of dry test piece, in grams
MDL-Loss	Loss in Mass, diameter and length loss calculation after durability test in %	M_h	Mass of test piece immersed in water, in grams
NDT	Non-Destructive Testing	M_s	Mass of saturated test piece, in grams
PM10	Particulate Matter 10(Suspended particles)	ϱb	Density in (gr/cm3)
XRD	X-Ray Diffraction	po	Open porosity in %
XRF	X-Ray Fluorescence	R	Rebound values
SEM	Scanning Electron Microscopy	V_p	Ultrasonic pulse velocity in km /s
SHM	Structural Health Monitoring	σ_c	Uniaxial compressive strength in MPa
SHR	Schmidt Hammer Rebound	σ_{caf}	Uniaxial compressive strength after durability test in MPa
TLS	Terrestrial Laser Scanning 3D	σ_f	Flexural strength in MPa

APPENDIX -A

Appendix A1: Climate data for the city of Tamentfoust

The analysis reveals a temperate Mediterranean climate, with an average temperature ranging from 11°C in February to 26.6°C in August. Summers (June–August) are hot, with temperatures exceeding 22°C, while winters (December–February) are mild, averaging 11–12°C. Summer thermal amplitude (13–14°C) is greater than in winter (11–12°C), reflecting more variable summer days, moderated by maritime influence (Fig. A1). Precipitation shows strong seasonality, being nearly absent in summer (1.6 mm in July) and abundant in autumn-winter (118.2 mm in November), with high variability (e.g., November: 21.3-253.4 mm). This pattern suggests intense and irregular rainfall episodes, likely linked to coastal storms, characteristic of a Mediterranean or oceanic climate. Humidity remains relatively stable, ranging from 70.3% in July to 80.9% in December, with a slight decrease in summer and an increase in winter, consistent with the site's coastal proximity (Fig. A1). Wind speed, averaging 8.9–11.4 km/h, suggests moderate exposure to prevailing winds, likely influenced by local topography.

Furthermore, statistical correlations reveal an inverse relationship between temperature and precipitation, reflecting hot, dry summers and mild, wet winters. The correlation coefficients between temperature and precipitation is equal to (-0.81), while a slight positive correlation between humidity and precipitation was obtained, with a coefficient of (+0.86). No evident connection was found between wind speed and other variables on a monthly basis, though daily data might provide further insight into wind patterns, particularly during storm events.

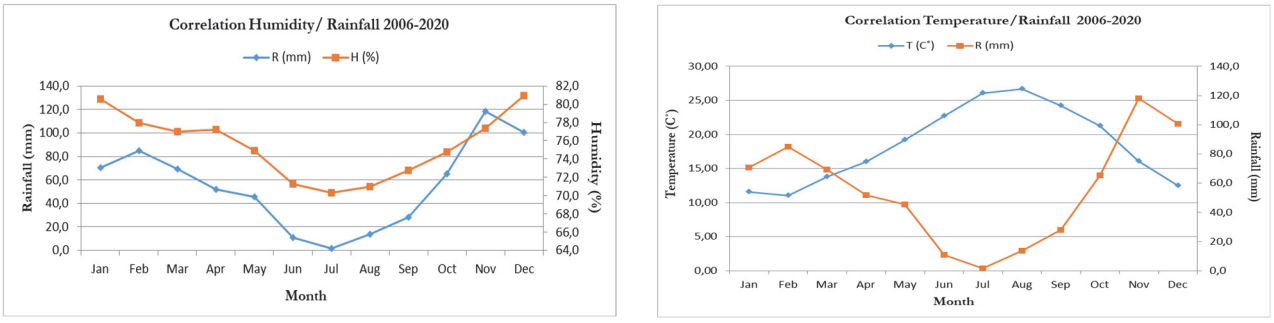

(a) (b)

Figure A1: (a) correlation between average annual humidity and average annual rainfall (b) correlation between average annual temperature and average annual rainfall.

Appendix A2: Test technical specifications.

A2-1: *X-ray diffraction (XRD) analysis*

- **Tools and software used**: For the XRD analysis, the procedure involved the use of the PDF-ICDD database and HighScore Plus software for diffractogram interpretation.
- **Objective**: The XRD analysis was employed to identify the crystalline phases present in the samples.

A2-2: *Scanning electron microscopy coupled with energy-dispersive X-ray spectroscopy (SEM-EDX) analysis*

- **Tools and software used**: For the SEM-EDX analysis, the procedure involved the use of a Zeiss Gemini 300 equipped with an Oxford X-MaxN 80 EDX detector, operating at accelerating voltages of 5–20 kV in variable pressure modes, with working distances of 5–15 mm.
- **Objective**: The SEM-EDX analysis was employed to characterize the surface topography, pore network architecture, and mineralogical constituents of lithic samples at nanoscale resolution (≤1 nm) with an elemental sensitivity of approximately 0.1 wt%.

A2-3: *X-Ray fluorescence (XRF) spectrometry analysis*

- **Tools and software used**: For the XRF analysis, the procedure involved the use of a SciAps X-200 spectrometer equipped with a high-performance silicon drift detector (SDD) with an active area of 20 mm^2 and a resolution of <140 eV FWHM at the 5.95 keV Mn K-alpha line, operating with a 40 kV Rh anode (for alloys) or a 50 kV Au anode (for geochemical, soil, RoHS, and other applications), achieving count rates exceeding 125,000 cps with >90% live time.
- **Objective**: The XRF analysis was employed to determine the elemental composition of the samples with high sensitivity.

A2-4: *Petrographic Analysis*

- **Tools and Software Used**: For the petrographic analysis, the procedure involved using polarized light microscopy (Leitz ORTHOPLAN, 40–1000×) to characterize the chemical and mineralogical composition of lithic specimens.
- **Objective**: The petrographic analysis was employed to reveal textural attributes, intragranular microporosity, bonding matrix integrity, and secondary mineralization phases, critical for understanding weathering mechanisms in heritage materials.

A2-5: *Porosity measurement*

- **Tools and software used**: For porosity measurement, the procedure involved drying samples at 70 ± 5 °C to constant mass (Md), followed by vacuum saturation at 2.0 ± 0.7 kPa for 2 ± 0.2 hours, and immersion in deionized water at 20 ± 5 °C for 24 ± 2 hours. Hydrostatic (Mh) and saturated (Ms) masses were measured.
- **Objective**: The porosity measurement procedure was employed to determine the porosity of the samples, as presented in Fig. A2-5.

(a) (b) (c) (d) (e) (f)

Figure A2-5: Test procedure: Open porosity and bulk density. (a) drying samples to constant mass,(b) weighing samples ($M_{d)}$,(c) samples in a vacuum vessel and reduction gradually of the pressure,(d) introduction slowly of demineralized water at (20 ± 5) °C until sample immersion ,(e) maintain a pressure of (2.0 ± 0.7) kPa ,(f) weighing the sample underwater ($M_{h)}$

A2-6: *Water absorption by atmospheric pressure*

- **Tools and software used**: For the water absorption by atmospheric pressure testing, the procedure involved drying samples to constant mass (md) and weighing them to the nearest 0.01 g. The samples were then placed in a reservoir on designated supports, ensuring a minimum distance of 15 mm between adjacent samples. Tap water at 20 ± 10 °C was added to half the height of the samples at time t0. At t0 + 60 ± 5 minutes, additional tap water was added to reach three-quarters of the sample height. At t0 + 120 ± 5 minutes, tap water was added to fully immerse the samples at a depth of 25 ± 5 mm. After t0 + 48 ± 2 hours, the samples were removed, quickly wiped with a damp cloth, and weighed within one minute to the nearest 0.01 g (mi). The samples were re-immersed, and the process was repeated every 24 ± 2 hours, with samples removed, wiped, and weighed to the nearest 0.01 g (mi). Successive masses (mi) were recorded until constant mass was achieved, defined as a difference between two consecutive weighings of ≤0.1% of the sample mass. The final weighing represented the saturated sample mass (ms) Fig. A2-6.
- **Objective**: The water absorption by atmospheric pressure testing was employed to determine the water absorption, expressed as a percentage, calculated as the ratio of the saturated sample mass (ms, obtained at constant mass) to the dry sample mass (md).

Figure A2-6: Different steps of the water absorption by atmospheric pressure

A2-7: *Capillary absorption measurement*

- **Tools and software used**: For the capillary absorption measurement, the procedure involved drying samples at 70 ± 5 °C to constant mass (Md), followed by immersion in water at a depth of 3 ± 1 mm. Water absorption (g/m²) was measured at intervals from 1 to 4320 minutes, with the test concluding when the difference between consecutive measurements was less than 1% of the total absorbed water.
- **Objective**: The capillary absorption measurement was employed to calculate the mean capillary absorption coefficients (C, mg/cm² s−½) from the slope of absorption versus t½, as presented in Fig. A2-7.

Figure A2-7: Water absorption by capillarity test.

A2-8: *Resistance to salt crystallisation test procedure*

- **Tools and software used**: For the salt weathering test, the procedure involved 15 cycles of immersion in 10% NaCl solution at 20 °C for 2 hours, drying at 105 °C for 16 hours, and cooling at 20 °C for 4 hours. Further analysis was performed using SEM-EDX, petrography, XRD, and XRF.
- **Objective**: The salt weathering test was employed to detect halite and evaluate deterioration through visual inspection, colour change, mass loss (%), dimensional variations, and reductions in compressive strength (σc, σcaf, Δσc), as presented in Fig. A2-8.

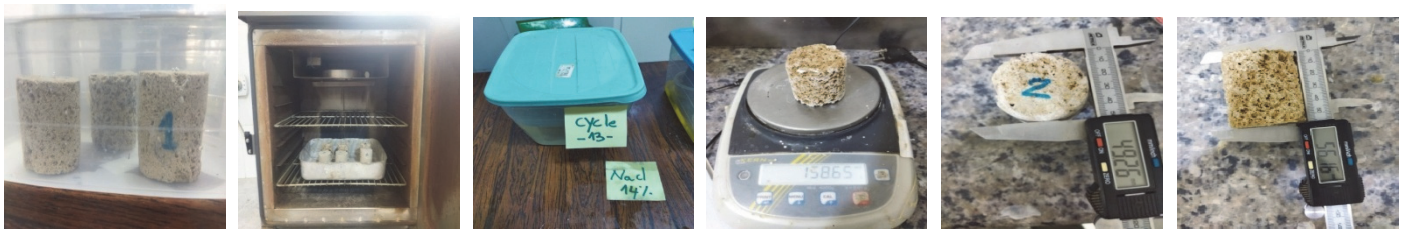

(a) (b) (c) (d) (e) (f)

Figure A2-8: Different steps of the resistance to salt crystallization test on the stone type T1-(a) immersion,(b) drying, (c) repeated cycles, and dimensional measurements taking before and after each cycle for PE1-5 / PE1-3 sample, for MDL-Loss calculation after salt crystallization test. (d) loss in mass (M), (e) loss in diameter(D), (f) loss in length (l).

A2-9: *Resistance to accelerated ageing by HCl*

- **Tools and software used**: For the accelerated ageing test by HCl, the procedure involved exposing samples to HCl over 21 days, with chemical and mineralogical analyses to assess degradation influenced by urban pollution in Algiers, including measured particulate matter (PM10: 122 µg/m³) and nitrogen dioxide (NO2: 91 µg/m³) levels.
- **Objective**: The accelerated ageing test by HCl was employed to assess mass loss, physical alterations (colour changes, cracks, etc.), and reductions in uniaxial compressive strength (σc, σcaf), as presented in Fig. A2-9.

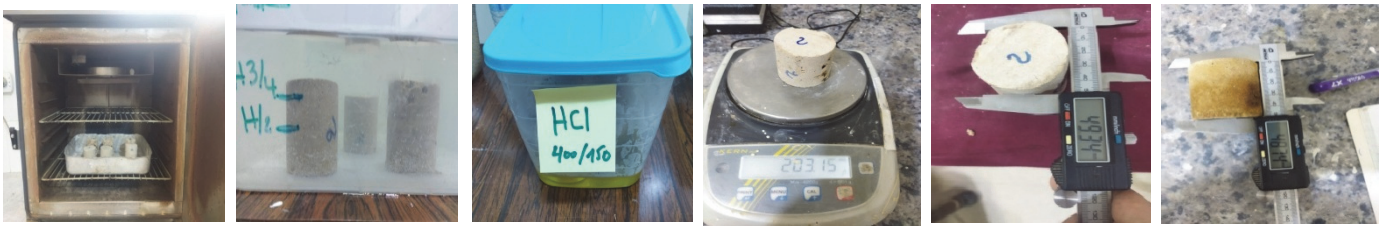

(a) (b) (c) (d) (e) (f)

Figure A2-9: Different steps of the determination of resistance to accelerated ageing with HCl in the presence of moisture- (a) samples washing and drying at 70C°,(b)samples water immersion during 24h,(c) sample placement in acid solution, and dimensional measurements taking before and after each cycle for PE2-6 / PE2-4 sample, for MDL-Loss calculation accelerated ageing with HCl. (d) loss in mass (M), (e) loss in diameter(D), (f) loss in length (l).

A2-10*: Ultrasonic pulse velocity measurement*

- **Tools and software used**: For the ultrasonic pulse velocity measurement, the procedure involved using a Pundit-Proceq tester (54 kHz, transducers: 24–250 kHz) in direct, indirect, and semi-direct modes, achieving a precision of ±1%. Measurements were conducted across sample separations of 80–270 mm, using a template and coupling gel to ensure accuracy.
- **Objective**: The ultrasonic pulse velocity measurement was employed to calculate the ultrasonic wave velocity (Vp), defined as Vp = L / T, where L is the known path length of the sample and T is the travel time of the ultrasonic wave, as presented in Fig. A2-10.

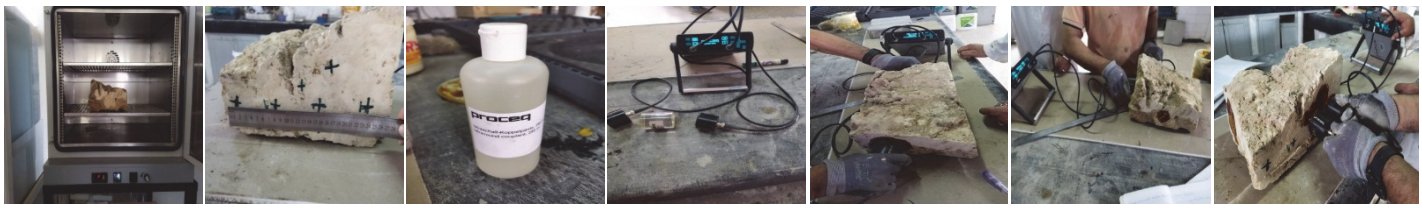

(a) (b) (c) (d) (e) (f) (g)

Figure A2-10: Different steps for the ultrasonic velocity test -(a) drying the tested block at a temperature of (70 ± 5) °C, (b) determination of reference points, (c)ultrasonic gel (d) Pundit-Proceq tester, and different transducer positions for determining the speed of sound propagation-(e) direct mode (f) semi direct mode (g) indirect mode.

A2-11: *Infrared thermography*

- **Tools and software used**: For the infrared thermography measurement, the procedure involved using a Fluke TIS50 camera with a temperature range of −20 to +450 °C, sensitivity of <0.08 °C at 30 °C, and resolution of 220 x 165 (36,300 pixels).
- **Objective**: The infrared thermography measurement was employed to diagnose material degradation and guide restoration efforts in heritage materials.

A2-12: *Schmidt hammer rebound (SHR)*

- **Tools and software used**: For the Schmidt Hammer Rebound (SHR) testing, the procedure involved using a Proceq Type N instrument with impact energy of 2.207 N.m and a range of 10–70 N/mm². A minimum of three readings was taken to calculate mean rebound values (R), with only readings within 7 units of the average considered, per ASTM D5873.
- **Objective**: The Schmidt Hammer Rebound (SHR) testing was employed to derive the compressive strength of limestone, ranging from 11 to 273 MPa, using an empirical correlation based on mean rebound values (R).

A2-13: *Mechanical tests*

Compressive strength testing

- **Tools and software used**: For the compressive strength testing, the procedure involved using a calibrated electromechanical (EM) universal machine MTS CRITERION C45 305E type with a maximum load capacity of 300 kN, at a load rate of 0.5–1 MPa/s. Six oven-dried samples with flat surfaces prepared with sulphur mortar to ensure uniform load distribution were tested, with tests repeated at least three times per stone type in accordance with EN 772-1.
- **Objective**: The compressive strength testing was employed to evaluate the compressive strength of stone samples under controlled loading conditions, as presented in Fig. A2-13.

Flexural strength testing

- **Tools and software used**: For the flexural strength testing, the procedure involved conducting tests under a centered load at 0.3 kN/s and a stress rate of 0.25 ± 0.05 MPa/s until failure, using symmetrically dried samples.
- **Objective**: The flexural strength testing was employed to determine the flexural strength of stone samples under centered loading conditions until failure as presented in Fig. A2-13 .

Figure A2-13: Mechanical tests

A2-14: *Crack measurement*

- **Tools and software used**: For the crack measurement and microstructural analysis, the procedure involved using a MATEST portable crackmeter (STDMC399) with a 360° rotatable eyepiece scale to measure cracks. Microstructural changes in four stone samples were analysed before and after aging durability tests.
- **Objective**: The crack measurement and microstructural analysis was employed to assess surface alterations due to mineralogical reactions in stone samples, as presented in Fig. A2-14.

(a) (b) (c) (d)

Figure A2-14: (a) the crackmeter from MATEST, (b) tested samples, before and after durability tests (c, d) the use of the crackmeter in the measurement of cracks development in the gallery support and the jointing mortar.

A2-15: Terrestrial laser scanning *(TLS)*

- **Tools and software used**: For the terrestrial laser scanning, the procedure involved using a FARO FOCUS scanner operating at 976,000 points/s, with an error of ±2 mm at 25 m and a field of view of 360° horizontally and 320° vertically, to capture geometric data of the Ottoman fort's façade across 40 scan positions. The resulting point cloud was processed using FARO Scene software to create a digital twin.
- **Objective**: The terrestrial laser scanning was employed to enable precise stonework mapping and create a digital twin of the Ottoman fort's façade.